Nuclear morphology and functional characteristics that enable survival of cells in the polyaneuploid cancer cell state following cytotoxic chemotherapy

Chi-Ju Kim[1,†], Anna LK Gonye[1,2,†], Kevin Truskowski[1,2], Cheng-Fan Lee[1], Kenneth J Pienta[1,2], Sarah R Amend[1,2]

Affiliations:

1. Cancer Ecology Center, The Brady Urological Institute, Johns Hopkins School of Medicine, 600 N. Wolfe St., Baltimore, MD, 21287, USA.

2. Cellular and Molecular Medicine Graduate Program, Johns Hopkins School of Medicine, 600 N. Wolfe St., Baltimore, MD, 21287, USA.

†. Contributed equally.

Abstract

The polyaneuploid cancer cell (PACC) state represents a recently-described paradigm in the study of therapy resistance. Cancer cells in this state are physically enlarged, acquire polyaneuploid genomes resulting from whole-genome doubling, and have been shown to be present in metastatic prostate cancer lesions as well as in the tumors of a variety of cancer types. Initiation of the PACC state begins when a cancer cell experiences a stressor, such as a genotoxic chemotherapy, and ends after a period of recovery following the release of the treatment cells exit the PACC state and resume proliferation to repopulate the tumor cell pool. One notable characteristic of cancer cells in the PACC state is their distinctive nuclear morphologies. Evidence in the literature demonstrates that abnormal nuclear morphology is associated with more aggressive metastasis and disease recurrence. We characterized nuclear morphology and function over time as prostate cancer cells underwent chemotherapeutic treatment and recovery to identify the unique characteristics that allow a cancer cell under stress to survive in the PACC state. We found that mononucleated cancer cells dominate the pool of cells in the PACC state that survive days after cisplatin treatment. Additionally, by examining markers of DNA damage and the DNA damage response, we found that cells that access the PACC state likely employ more successful DNA damage repair. Lastly, while many prostate cancer cells treated with a genotoxic agent succumb to apoptosis in the days following treatment release, our data suggest that surviving cancer cells must regulate a balance autophagy levels to restore cellular homeostasis while not initiating autophagic cell death. Together, our findings present a course of events that take place as a treated cancer cell recovers from chemotherapy and access the PACC state, representing an important set of findings to the understanding of therapy resistance and recurrence.

Introduction

Once cancer has metastasized, it is incurable because tumors evolve resistance to virtually all systemically administered anticancer therapies. Classically, resistance to therapy has been largely attributed to the presence of cancer stem cells or genetically heterogeneous subsets of cancer cells within the tumor, which allow for continued survival of a cancer cell population due to the presence of a resistant clone or clones[1-22]. However, our group and others have identified a stress-induces cell state characterized by physical enlargment and polyaneuploid genomes. Cells in the polyaneuploid cancer cell (PACC) state have been identified in the tumors of patients with metastatic prostate cancer (PCa), as well as in other tumor types[23-33]. Presence of cells in the PACC state in clinical radical prostatectomy specimens from PCa patients is predictive of an increased risk of disease progression[34]. The PACC state is initiated when a cancer cell is subjected to a stressor, such as chemotherapy or radiotherapy, triggering a conserved evolutionary program that results in sustained polyploidization of the aneuploid genome (polyaneuploidy) and increased cell size and cell contents. When the cellular stressor is no longer present and after a period of recovery, a subpopulation of cells may exit the PACC state and reinitiate proliferation, a phenomenon clinically observed as cancer recurrence[23-33,35-42].

The PACC state is the result of a noncanonical cell cycle that bypasses cell division in response to environmental stress[25,43-47]. Skipping mitosis and/or cytokinesis results in the increase of cellular contents, including nuclear size and genomic material, and is hypothesized to aid the cell in adapting to toxic

environments such as therapeutic stress[23,26,28,31,32]. Additionally, the increased genomic content may help prevent cells in the PACC state from undergoing cell cycle checkpoint-activated apoptosis due to DNA damage[23-31,33,35-42,48,49]. The abnormal, amitotic cell cycle that creates the genomic duplication characteristic of the PACC state can be characterized as mitotic slippage, endocycling, or endomitosis[50-53], and is accompanied by abnormal nuclear morphologies including large mononucleated, mononucleated and simultaneously lobulated, or multinucleated phenotypes[26-31,42,48]. It is likely that the specific nuclear morphology of PACCs plays a role in the survival and eventual formation of progeny by these cells.

Abnormal nuclear morphology is often conspicuous in cancer cells[54-64]. The precise underlying mechanisms resulting in the morphological abnormality of nuclei in cancer cells are still under study. Such phenotypes may arise from the intrinsic physiological properties of cancer cells (i.e., the dysregulation of the cell cycle) and cause aneuploidy, genomic instability, and abnormal gene and protein expression patterns including genomic alterations of nuclear envelope-associated proteins[64]. It has often been shown that irregular and large nuclear shapes reflect malignancy in cancer[55,57,62-64]. Historically, an increased variation in nuclear size and shape has been regarded as a significant pathologic parameter and used clinically for the diagnosis of various cancers[64,65]. Hyper-abnormal nuclear morphologies, such as multilobulated and multinucleated nuclei, are highly associated with metastasis and recurrence[35,55,66]. Since cancer cells in the PACC state exhibit most or all of these distinct nuclear shapes associated with malignancy[55,57,62-64] and because recent evidence suggest that the PACC state could be the lynchpin of cancer lethality[23-31,33,35-42,48], it is important to investigate the timing and mechanisms utilized by cancer cells to enter and maintain the therapeutic resistant PACC state.

As a starting point of our exploration into the biology of the PACC state, in particular the life history of cells following chemotherapy treatment that successfully access the PACC state versus those that die after chemotherapy, we performed a characterization of nuclear morphology and function over time following treatment release. For the first time, we demonstrate that mononucleated polyploid cells dominate the population that survive the weeks following therapy, and thus represent a strong candidate to eventually seed therapeutic resistant population (**Fig. 1**). Taken together, these data indicate that cells that survive cisplatin treatment access a mononucleated PACC state continues to replicate DNA via endocycling and retains high levels of DNA damage repair, while multinucleated cells that initially survive therapy eventually undergo autophagic cell death.

Experimental methods

Cell culture

PC3 and DU-145 prostate cancer cell lines and the breast cancer cell line MDA-MB-231 were originally purchased from ATCC (United States). Cell lines were maintained in RPMI Medium 1640 with L-Glutamine (for PC3 and DU-145 cells; Gibco, #11875-093) or DMEM (for MDA-MB-231 cells; Gibco, #11995-065), both supplemented with 10% fetal bovine serum (FBS; Avantar, #97068-085) and 1% penicillin streptomycin (Gibco, #15140-122). Cells were cultured in standard conditions: 37 °C, 5% CO_2. All cells were routinely checked for mycoplasma via LabCorp's RT-qPCR mycoplasma contamination detection service.

Treatment

Sub-confluent cultures of PC3 cells were treated with [LD50] concentrations of cisplatin (6 µM; Millipore Sigma, # 232120-50MG), docetaxel (5 nM; Cell Signaling Technology, # 9886), or etoposide (25 µM; Cell Signaling Technology, #2200S) and cultured for 72 hours under standard conditions. DU-145 and MDA-MB-231 cell lines were treated with cisplatin [LD50], with concentrations of 2 µM and 12 µM, respectively. To capture cells with the potential to enter the PACC state, large cells were then sterilely isolated via size-restricted filtration with a pluriStrainer® 15 µm cell strainer (pluriSelect, #45-50015-03) and subsequently replated for culturing.

Nuclear morphological analysis

Large cells were generated as described and then cultured for 1, 5, 10, and 15 days after being filtered following 72 hours of drug treatment. 24 hours prior to each timepoint, the cells were seeded into 35 mm IbiTreat μ-Dishes (Ibidi USA, Inc., #81158) and incubated overnight. Samples were then fixed in 10% formalin for 20 minutes, and permeabilized for 10 minutes in 0.2% (v/v) of Triton-X-100 diluted in phosphate-buffered saline. Permeabilized samples were blocked with 10% (v/v) goat serum in PBS at room

temperature for 30 min. Samples were then incubated overnight at 4 °C with anti-lamin A/C mouse mAb IgG2a (Cell Signaling Technologies, #4777) diluted 1:100 in blocking buffer. Following staining, samples were incubated with Alexa Fluor™ 488 goat anti-mouse IgG2a secondary antibody (Invitrogen, #A21121) diluted 1:1000 in blocking buffer for 1 hour at room temperature, protected from light. Finally, each sample was mounted with ProLong™ Diamond Antifade Mountant with DAPI (Invitrogen, #P36971) and images were acquired using a Zeiss Observer Z1 microscope and ZEN pro 2.0 software (Carl Zeiss Microscopy). Nuclear morphology (mono-nucleated vs. multi-nucleated) was manually discriminated and counted using Fiji[67].

Nucleolar morphological analysis

Large cells were induced, seeded, fixed, permeabilized, and blocked as described above. The samples were incubated with 1:50 Alexa Fluor™ 647-conjugated anti-nucleolin antibody (Abcam, #ab202709), and 1:100 anti-lamin A/C mouse IgG2a mAb (see above) diluted in blocking buffer, overnight at 4 °C. Following primary staining, samples were incubated with Alexa Fluor™ 488 goat anti-mouse IgG2a secondary antibody (see above) diluted 1:1000 in blocking buffer for 1 hour at room temperature, protected from light. Samples were mounted and images were acquired as described above. Finally, Images were analyzed for nucleolar number and area via a custom CellProfiler 4.0[68] pipeline.

Nuclei isolation

Cells were lifted and washed twice with PBS and then stored on ice. Nuclei extraction buffer (NEB) was also prepared on ice and consisted of final concentrations of 10 mM HEPES (Life Technologies Corp., #15630-080), 1.5 mM $MgCl_2$, 10 mM KCl, 0.25% NP-40 (Thermo Scientific, #95124), and 1X protease/phosphatase inhibitor (Thermo Scientific, #1861281) diluted in ultrapure deionized water. Per $1x10^6$ cells, 500 μL of NEB was added, and samples were mixed six times via pipetting, and then placed on ice for 10 minutes. Samples were then spun down for 10 seconds in a compact benchtop centrifuge, and the supernatants containing cytoplasmic components were removed. This was repeated twice more, with 5-minute incubations on ice. Following the final removal of supernatants, samples were resuspended in 10% formalin, incubated at room temperature for 10 minutes, and then filtered through a 70 μm cell strainer. The fixed and filtered nuclei were then spun down with a quick spin, formalin was removed, and nuclei were resuspended in PBS. Nuclei suspensions were then allowed to adhere to Ibidi μ-Dishes (glass bottom, Ibidi, #81158) pre-coated with Poly-L-Lysine (EMD Millipore Corp., #A-005-C) for 30 minutes at room temperature. Once any non-adhered nuclei were washed away, samples were permeabilized with 0.5% Triton-X 100 in PBS and subsequently stained for immunofluorescence imaging, then covered with ProLong™ Diamond Antifade Mountant with DAPI (Invitrogen, #P36971). Images were analyzed for nuclear area via a custom CellProfiler 4.0 pipeline (see above).

DNA damage response marker foci analysis

Large cells were induced, seeded, fixed, permeabilized, and blocked as described above. Then, samples were incubated overnight at 4 °C with 1:250 anti-gamma H2A.X mouse IgG1 mAb (Abcam, #ab22551), 1:100 anti-53BP1 rabbit mAb (Abcam, #ab175933), and 1:100 anti-lamin A/C mouse IgG2a mAb (see above), followed by washes with 0.1% (v/v) PBS-T. Appropriate secondary antibodies, 1:1000 Alexa Fluor™ 488 goat anti-mouse IgG1 mAb (Invitrogen, #A21121), 1:1000 Alexa Fluor™ 594 goat anti-rabbit IgG (H+L) (Invitrogen, #A32740), Alexa Fluor™ 647 goat anti-mouse IgG2a mAb (Invitrogen, #A21241), were conjugated with primary antibody for 1 hour at room temperature, followed by five washes with 0.1% (v/v) PBS-T. Both primary and secondary antibodies were diluted with 1% (v/v) BSA in 1X PBS. Fluorescently labeled cells were mounted using ProLong™ Diamond Antifade Mountant with DAPI (Invitrogen, #P36971). Image acquisition was performed using a Zeiss Observer Z1 microscope and ZEN pro 2.0 software (Carl Zeiss Microscopy). Images were analyzed via a custom CellProfiler 4.0 pipeline (see above).

Three-dimensional (3D), confocal, live-cell imaging

Live cells were incubated for 45 minutes at standard conditions with 1 μg/mL of CellTracker™ Orange CMTMR (Invitrogen, #C2927) and 10 μM Vybrant™ DyeCycle™ Green Stain (Molecular Probes, # V35004) to label the cytoplasm and nucleus, respectively. Labeled cells were lifted and resuspended in cold Matrigel Basement Matrix (Corning, #356232). This cell suspension was plated onto 35 mm glass bottom μ-Dishes (Ibidi USA, Inc., #81158) and immediately coverslipped. Plated samples were cultured for 30 minutes at standard condtions to allow for solidification of the Matrigel, and then were covered with

phenol-free RPMI Medium 1640 with L-Glutamine (Gibco, #1835030) supplemented with 10% fetal bovine serum and 1% penicillin streptomycin). Image acquisition was performed using a Nikon Eclipse Ti2 microscope with a Nikon C2 camera and NIS Elements version 5.11. (Nikon Inc.) with a live-cell imaging ThermoBox incubation system (Tokai Hit Co.). All 3D image processing and analysis was performed with Imaris 9.8 software (Oxford Instruments).

Western blotting

Cells were lysed in ice-cold lysis buffer [150 mmol/L NaCl, 1% Triton X-100, 0.5% sodium deoxycholate, 0.1% SDS, 50 mmol/L Tri (pH 8.0), protease inhibitor cocktail (Roche)], and cell debris was removed by centrifugation at 4 °C for 10 min at 12,000 rpm. Equal amounts of protein were subjected to electrophoresis on SDS-PAGE gels (Bio-Rad Laboratories, #4561095) and transferred onto Trans-Blot Turbo nitrocellulose membranes (Bio-Rad Laboratories, #1704158). Subsequently, the membranes were blocked with 1X casein blocking buffer (Sigma–Aldrich, #B6429,) for 1 hour at room temperature. Once blocked, the membranes were incubated with primary antibodies against phospho-histone H2A.X (1:1000; Cell Signaling, #9718), Histone H2A.X (1:1000; Cell Signaling, #7631), Lamin A/C (1:1000; Cell Signaling, #4777), 53BP1 (1:1000; Abcam, #ab175933) and β-Actin (1:10000; Millipore Sigma, #A5441,). Secondary antibodies included IRDye 680RD goat anti-mouse (1:20,000; LI-COR Biosciences, #926-68070) and IRDye 800CW goat anti-rabbit (1:15,000; LI-COR Biosciences, #926-32211. Blots were imaged on a LICOR Odyssey. Results were quantified by ImageJ software, and the relative protein expression level in each sample was normalized to the internal control.

FUCCI cell line generation

$1.5x10^6$ HEK-293T cells were plated in 10 cm dishes in DMEM supplemented with 10% FBS. After 24 hours, cells were transfected for second generation lentivirus packaging as follows: 1 µg of Ki67p-T2A-FUCCI plasmid[69] (gifted from Alexander Zambon) and 1 µg of psPAX2:pMD2.g (packaging:envelope) at an 8:1 ratio were diluted in 200 µL of OptiMEM media (Gibco, #31985062). Both psPAX2 (Addgene plasmid #12260; http://n2t.net/addgene:12260 ; RRID:Addgene_12260) and pMD2.g (Addgene plasmid #12259; http://n2t.net/addgene:12259 ; RRID:Addgene_12259) were a gift from Didier Trono. 5 µL of X-tremeGENE HP transfection reagent (Roche, #XTGHP-RO) was added, and the solution was mixed by pipetting and incubated for 30 minutes before being added dropwise onto the HEK-293T. After 18-20 hours, media was changed to the target cell media supplemented with 30% heat inactivated FBS. Packaging cells were allowed to condition media for 48 hours before viral harvest. Viral media was removed and filtered through a Millex HP 0.45 µm PES syringe filter (Millipore, #SLHPM33RS). Lentivirus from 1-2 10 cm dishes (10-20 mL) was concentrated using Clontech Lenti-X concentrator (Takara, #631232) per the manufacturer's protocol. The viral pellet was resuspended in target cell media supplemented with 30% heat inactivated FBS and added onto PC3 cells ($3.5x10^5$/well) in 6-well plate along with 10 µg/mL Polybrene Infection Reagent (Millipore, #TR-1003). PC3 cells were transduced for ~20 hours before media was changed to fresh supplemented RPMI. After 3 days of recovery, cells were selected with 5 µg/mL blasticidin (Gibco, #A1113903) and expression of reporters was assessed on an EVOS FL Auto imaging system (Life Technologies) with GFP (for mAG) and TxRed (for mCherry) light cubes. Clones were generated from the selected cell pool via limiting dilution cloning.

Time-lapse imaging of PC3-FUCCI

$8x10^4$ PC3-FUCCI cells were plated per well in a 6-well plate and cultured overnight under standard conditions. Cells were then treated with 6 µM [LD50] cisplatin for 72 hours to induce accession of the PACC state. After treatment, media was changed to fresh RPMI and live-cell timelapse microscopy of PACCs was performed in an Incucyte SX5 (Sartorius). Images were taken every 30 minutes in the phase, green, and orange channels.

EdU incorporation assay

16, 13, 9, 7, or 5 days before endpoint, $7.5x10^6$ PC3 were plated in T75 flasks and left to adhere overnight. The following day they were treated with 6 µM [LD50] cisplatin. After 72 hours of treatment, the induced PACC cells were lifted, and $3x10^4$ cells were plated on 12 mm round coverslips in 24-well plates. Once cells adhered, the media was replaced and supplemented with 10 µM EdU (Molecular Probes, #E10187). After a 20-hour incubation period under standard conditions, the Click-It Plus EdU assay (Molecular Probes, #C10640) was performed according to the manufacturer's protocol. Coverslips were mounted to slides using ProLong™ Diamond Antifade Mountant with DAPI. Tiled images (12x12 tiles) were acquired using the 10x objective on the Zeiss Observer Z1 microscope and ZEN pro 2.0 software (Carl Zeiss

Microscopy). A custom CellProfiler pipeline was developed and used to quantify total number of nuclei in the tiled image based on DAPI signal and number of EdU-positive nuclei based on AlexaFluor™ 647 signal within nuclei boundaries.

Flow cytometry analysis

To label autophagosomes, live cells were incubated with an Autophagy Assay Kit (Red) (Abcam, #ab270790) according to the manufacturer's recommendation. To label apoptotic cells, live cells were incubated with FITC-Annexin V (BioLegend, #640906) for 15 minutes at room temperature according to the manufacturer's protocol. These fluorescently labeled cells were analyzed directly following labeling on an Attune NxT Flow Cytometer (Thermo Fisher Scientific). The BL1 channel (488 nm laser, 530/30 nm emission filter) was used to detect FITC-Annexin V-labeled apoptotic cells, and the YL2 channel (561 nm laser, 620/15 nm emission filter) was used to detect autophagosome- and autolysosome-abundant cells. At least 40,000 events were recorded per sample, and the acquired data was analyzed using FlowJo software version 10.8. (BD Biosciences).

Immunofluorescent imaging of autophagosomes

Cells were seeded into 35 mm IbiTreat μ-Dishes and cultured overnight. The cells were then fixed and permeabilized as described above. Following permeabilization, samples were blocked with 10% (w/v) BSA (Millipore Sigma, A9418) for 30 minutes. The samples were then incubated overnight at 4 °C with primary antibodies, diluted in block, against LC3A/B (1:100, Cell Signaling Technology, #12741), lamin A/C (1:100, see above), and gamma H2A.X (1:250, see above) and subsequently washed with 0.1% (v/v) PBS-T. Appropriate secondary antibodies, Alexa Fluor-488 (1:1000; Invitrogen, #A21121), Alexa Fluor-594 (1:1000; Invitrogen, #A32740), and Alexa Fluor-647 (1:500; Invitrogen, #A21241) were diluted in block and conjugated with primary antibody for 1 hour at room temperature, followed by washes with PBS-T. Fluorescently labeled cells were mounted with ProLong™ Diamond Antifade Mountant with DAPI. Images were acquired using a Zeiss Observer Z1 microscope and ZEN pro 2.0 software (Carl Zeiss Microscopy).

Autophagosome detection by 3D live-cell imaging

Live cells were labeled with 2 μM Calcein AM (Invitrogen, #C3100MP) for cytoplasm and Autophagy Assay Kit (Red) (Abcam, #ab270790) for 30 minutes under standard culture conditions as recommended by the manufacturer. These reagents were diluted in Hanks' Balanced Salt solution (HBSS; Gibco, #14025-092). Labeled live cells were washed with HBSS, and phenol red-free media was added to culture dishes prior to imaging. Image acquisition was performed using a Nikon Eclipse Ti2 microscope with a Nikon C2 camera and NIS Elements version 5.11. (Nikon Inc.) with a live-cell imaging ThermoBox incubation system (Tokai Hit Co.). Image processing and analysis was performed with Imaris 9.8 software (Oxford Instruments).

Ribosomal RNA gel electrophoresis

Total RNA was isolated from parental PC3 cells or PACCs using the PureLink™ RNA Mini Kit (Invitrogen, # 12183025). A mass of 100 ng total RNA was prepared for gel electrophoresis and run on a 1% agarose-TBE gel with ethidium bromide. Gels were imaged on a Bio-Rad ChemiDoc™ XRS+ and 28s, 18s, and 5.8s ribosomal RNA bands could be observed.

Statistical analysis

All statistical analyses were performed in GraphPad Prism version 9.1 (GraphPad Software, LLC). An $\alpha = 0.05$ (confidence level 95%) was the criterion considered to determine statistical significance for all tests. No significance (ns), *, **, ***, and **** represent p values of >0.05, <0.05, <0.01, <0.001, and <0.0001, respectively.

Results

Classification of nucleus morphology in cancer cells following treatment release

Cancer cell lines were treated with [LD50] concentrations of cisplatin for 72 hours, and then treated cells were allowed to recover for various time periods following replacement of the culture media. We observed the expected cell die off at 72 hours. All following studies were performed on the surviving cell populations at each time point. First, we classified the morphology of treated cancer cell nuclei into two categories: mononucleate and multinucleate. The treated cancer cell nuclear morphology was visualized by immunofluorescent imaging in both 2D (**Fig. 2A**) and 3D (**Fig. 2B**). Conventional nuclear visualization in 2D by DNA staining with DAPI or Hoechst is not always suitable for distinguishing between types of nucleus

morphology (**Fig. S1**), but additional labeling of nuclear structures enhances the visualization to discriminate nuclear morphology. The nuclear envelope (NE) of cells was visualized by performing immunofluorescent labeling of lamin A/C, an abundant structural component of the NE (**Fig. 2A**). Immediately after removal from cisplatin treatment, treated PC3 cells exhibited a uniformly distributed morphology, with the proportion of mono- and multinucleates each approximately 50% (**Fig. 2A, C**). As PC3 cells recovered, the population ratio shifted, with mononucleates becoming predominant as the recovery time was prolonged (**Fig. 2C**), which conversely indicates that multinucleated treated cells are not viable and eventually die. Our 2D methodology underestimated the number of multinucleates at the early time points due to a spatially hindering effect of the nuclear envelope signal (**Fig. S12**). We therefore confirmed this finding by 3D confocal microscopy imaging of treated nuclei (**Fig. 2B, D**). Live cells were embedded in Matrigel to maintain their cellular structure and prevent cell flattening, and their nuclei and cytoplasm were fluorescently visualized. The Imaris software platform enabled the reconstruction of 3D nuclear structure, and the distributions of nuclear morphology at various points in recovery were determined. The trend of shifting to a prevalence of mononucleate morphology in the recovered PACC population was consistent between the 2D and 3D analyses (**Fig. 2D**).

Characterization of nuclear and cell size following treatment release

We characterized how treated cell volume and nuclear volume changed over time by assessing cytoplasmic and nuclear volumes measured by 3D confocal microscopy. We observed that the nuclear volumes of surviving cells continuously increased as a function of recovery time (**Fig. 3A**). Additionally, nuclear volume increased in correlation with increased cell volume (**Fig. 3A, B**). To determine the extent to which the nuclear size was influenced by cytoskeletal or other cytoplasmic components, we measured the area of isolated nuclei. The nuclear envelope of the isolated nuclei was fluorescently labeled with an anti-lamin A/C antibody and visualized with immunofluorescence microscopy, along with DNA contents (DAPI) (**Fig. 3C, D**). Consistent with whole-cell data, the size of isolated nuclei increased as a function of the recovery time, corresponding with the nuclear volume data from whole, intact cells (**Fig. 3D**).

Cancer cell endocycling increases nuclear size

The characterization of the nuclear morphology and size of the surviving cells suggested that mononucleated cells may undergo repeated DNA duplication during the recovery period following cisplatin treatment. We tested this hypothesis via two distinct and complementary assays: a fluorescence ubiquitination cell cycle indicator (FUCCI) cell cycle sensor assay (see FUCCI construct, **Fig. S2**) and an EdU assay. The nuclei of cells transduced the FUCCI construct will fluoresce red in G1, yellow (double positive for red and green) in very early S, green in mid-late S and G2, and are colorless in M and G0. Using live cell imaging, we observed large cisplatin-treated cells cycling through these different fluorescent stages, indicating that the surviving mononucleated cells underwent endocycling (**Fig. 3E**). To specifically test DNA replication, cultures were pulsed with EdU for 20 hours and EdU incorporation was visualized with immunofluorescence imaging (**Fig. 3E, F**). The EdU assay showed that mononucleated cells were actively engaging in *de novo* DNA synthesis at all timepoints following removal of cisplatin (**Fig. 3F**). These findings indicate that surviving cells, while not proliferative, are functionally active in genome duplication, although certain cellular behaviors (i.e., lack of division) suggest some type of temporary functional dormancy.

We further investigated the qualitative 3D morphological features of post-treatment PC3 nuclei. The nucleus-to-cytoplasm ratio (NC ratio) gradually decreased as a function of recovery time (**Fig. 3G**). This result implies that the rate of non-nuclear biomolecules is relatively faster than genomic replication compared to treatment naive cells. We also determined the sphericity of nuclei of treated cells and observed that it gradually decreased as a function of recovery time (**Fig. 3H, Fig. S3**), suggesting that nuclei at later time points may exhibit low rigidity or high deformability, perhaps due to a lower supporting force derived from their cytoskeleton[55,62,70-73].

Nucleolar size and number following cisplatin treatment

The nucleolus, the largest organized substructure of the nucleus, acts as a ribosomal RNA production hub and plays a significant role in nuclear homeostasis[74-77]. It has been reported that the size and number of nucleoli are highly correlated with enhanced cancer cell proliferation, growth, and malignancy in cancer[74-80]. We investigated differences in nucleolar structure between non-treated cancer cells and cancer cells at different timepoints following cisplatin therapy (**Fig. 4**). Interestingly, the number of nucleoli within the nuclei

of treated PC3 cells decreased (**Fig. 4A, B**), while the average size of each nucleolus increased (**Fig. 4A, C**) over time. Additionally, the nucleolus to the nucleus ratio in treated cells initially decreased at the early time point (until day 3) and rebounded during recovery (**Fig. 4D**). Western blotting to evaluate nucleolar marker (p-NPM, phosphorylated nucleophosmin) expression provided further supports this finding (**Fig. 4E**). These results indicate that the synthesis of nucleolar molecules was slower than that of nuclear molecules in treated cells; however, nucleolar size appears to return to relative levels similar to untreated controls. This suggests the potential of nucleoli to actively respond to genomic stress during treatment recovery to maintain nuclear homeostasis [76,77,79-81].

In its function as a ribosomal RNA production hub, a nucleolus contains genes for rRNAs, including 5.8S, 18S, and 28S rRNAs, that are transcribed as a single unit within the nucleolus[74-77]. RNA gel electrophoresis showed that the level of 28S rRNA in treated PC3 cells was higher than that of parental cells and increased as a function of recovery time. The level of 18S rRNA was lower in the treated cells. The level of 5.8S rRNA decreased in the treated cells until 10 days after therapy release (**Fig. S4**). The altered rRNA composition of cells recovering from cisplatin treatment suggests that the remodeling of rRNA configuration in the nucleolus may be a response to genomic stress to restore cellular function.

Quantification of DNA damage responses in the PACC state

Following release of [LD50] cisplatin treatment, we found that treated cells continuously underwent cell death (**Fig. 5A**), and the death rate gradually decreased as a function of recovery time and reached a plateau (**Fig. 5B**). The DNA damage response (DDR) plays a crucial role to avoid programmed cell death and prolong cellular life[82,83]. To investigate the relevance of the DDR to cell survival and death as cells accessed the PACC state, the expression of DDR markers (i.e., gh2ax and 53BP1) was analyzed (**Fig. 5C-G**). gh2ax foci expression represents DNA damage loci, whereas 53BP1 molecules are recruited to DNA damage to initiate the DNA repair pathway, forming distinct foci at sites damaged DNA loci[82,83]. Defective recruitment of 53BP1 to damaged DNA can result in DDR failure, eventually inducing cell death[82,84-87]. Colocalization of gh2ax and 53BP1 foci was assessed for each recovery time point (**Fig. 5D**). Treated PC3 cells early time points following therapy (days 1 and 3) had a low level of colocalization, but the colocalized gh2ax/53BP1 foci returned to the level of the untreated cancer cell control at day 10 post-treatment. These findings suggest that surviving cells activate the DDR pathway to avoid cell death.

The absolute value of gh2ax and 53BP1 foci counts per nuclei area were also calculated (**Fig. 5E, F**). Excessive DNA damage induces acute apoptosis and exhibits a distinct gh2ax expression pattern called gh2ax pan-staining[88-90]. Pan-stained nuclei were evaluated independently and excluded from the foci counts to avoid artifacts of extreme foci counts. The proportion of gh2ax pan-stained nuclei in treated cells was approximately half of the total population at day 1 and still 30% at day 3, gradually decreasing during the remaining of the recovery points examined (**Fig. S5**). The exclusion of many pan-stained nuclei in the early recovered PACC population led to a highly underscored absolute value of gh2ax foci, especially day 1 and day 3, exhibiting relatively low counts, which is not represented in the colocalization ratio (**Fig. 5D**). The pan-stained nuclei for 53BP1 expression were not observed; thus, the absolute value of 53BP1 foci counts per area itself indicates that they decreased until day 3 and increased to pre-treatment levels by the later treatment recovery timepoints (**Fig. 5F**).

Mononucleate cells became the dominant population over the duration of treated cell recovery (**Fig. 2C**), and, conversely, this indicates that multinucleated cancer cells died. To investigate the relevance of these two nuclear morphologies in the function of the DDR, the level of colocalization between gh2ax and 53BP1 foci in each types was compared (**Fig. 5G**). Mononucleate cells contain more colocalized DDR foci than multinucleates, indicating that the maintenance of single, large nucleus is a key feature of the resilient surviving cancer cells.

The mechanism of death in cells following treatment

The level of apoptosis in the treated cells was initially assessed by annexin-V assay by flow cytometry analysis. As expected, the annexin-V staining was higher in the treated cells but signal reduced with increased recovery time out to three days post-treatment (**Fig. 6A**). These data indicate that the relative level of apoptotic cell death decreases during recovery and suggest that apoptosis is unlikely to be the predominant cell death mechanism in cells that initially survive the cisplatin therapy.

Autophagy has been regarded as a cell survival program that helps to maintain cellular homeostasis[91-96]. However, evidence in the literature suggests that autophagy can also play a role in cell death. Broadly, autophagic cell death is a type of cell death that is accompanied by high amounts of autophagic vacuolization of the cytoplasm, often in the absence of complete chromatin condensation[97]. By flow cytometry using a reagent that specifically labels autophagosomes and autolysosomes, we found that treated cancer cells had increased levels of autophagy compared to treatment-naïve controls, and that this level increased with time post-treatment removal (**Fig. 6B**). We further investigated the level of autophagy at the prolonged recovery time points (days 5 and 10) by visualizing autophagosomes and/or autolysosomes via immunofluorescence microscopy (**Fig. 6C**). The volumetric quantification of autophagic vesicles inside cells via 3D confocal microscopy (**Fig. 6D, E**) demonstrated that the level of autophagy rapidly increased immediately after treatment and gradually increased during recovery (**Fig. 6F**). Since the cellular volume of treated cells continuously increased (**Fig. 3B**), the number of autophagosomes was normalized to cellular volume. The number of autophagosomes per unit volume increased until day 3 of the recovery period and was saturated until day 10 (**Fig. 6G**). Interestingly, the size of autophagosomes also increased as a function of recovery time (**Fig. 6H**). The increased autophagy was also confirmed by measuring the expression of autophagy markers (LC3B-I and LC3b-II) by western blot (**Fig. 6I, J**). The result was consistent with the autophagosome counts, thus supporting that the level of autophagy in surviving cells post-treatment is significantly higher than that of the parental cell population.

We hypothesized that nucleophagy, or the autophagy of genomic contents, might contribute to increased levels of autophagy over recovery time since one of observed phenotypes at early time points in recovery is that cells contain micronuclei and fragmented cytoplasmic DNA[98-101]. We performed immunofluorescence imaging where we labeled autophagosomes by staining for LC3B, a representative autophagy marker, while simultaneously probing for gh2ax, lamin A/C (nuclear envelope), and DAPI (**Fig. 6K**). Cells undergoing nucleophagy were readily observed in the treated population 3 days post-treatment, which indicates that excessive nucleophagy at the early time point of recovery may contribute to autophagic cell death. Of note, the portion of multinucleated cells dramatically decreases after day 5 of the recovery period, converse to the pattern of increasing autophagosome counts per volume.

Consideration of the cell-line heterogeneity and drug-type dependency

To identify cell type- and drug-specific phenotypic responses to treatment and recovery, we assessed breast cancer cell line MDA-MB-231 and treatment with common chemotherapies docetaxel (microtubule stabilizer) and etoposide (topoisomerase II inhibitor).

MDA-MB-231 breast cancer cell line exhibited a different pattern of nuclear morphology after treatment with [LD50] cisplatin in which the proportion of multinucleated cells increased during recovery (**Fig. S6**). When we investigated the DDR in this MDA-MB-231 treated population, we observed that the colocalization ratio of gh2ax and 53BP1 was initially high at day 1 but decreased until day 5 before returning to an elevated level in the recovered population by days 10 and 15 post-therapy removal (**Fig. S5**). The ratio of gh2ax pan-stained nuclei was lower in treated MDA-MB-231 cells than in PC3 cells at day 1 of the recovery period (**Fig. S5**). The absolute values of both gh2ax and 53BP1 counts per area gradually decreased during recovery (**Fig. S7**). Notably, most parental cells do not express both gh2ax and 53BP1 foci. It was also confirmed that the level of DDR in mononucleated cells was higher than that in multinucleated cells (**Fig. S7, Fig. S8**). Taken together, the initially active DDR in treated MDA-MB-231 cells may result in the delay in the formation of multinucleate cells in this cell line model. Consequently, the relative number of surviving MDA-MB-231 cells at each recovery time point was higher than observed in PC3 (**Fig. S9**), so the death rate was lower at early time points of the recovery period (**Fig. S9**).

A primary mechanism of multinucleate formation is a mitotic catastrophe[26,27,31,48,102-106]. The proportion of nuclei that underwent a mitotic catastrophe in both PC3 and MDA-MB-231 was determined by examining immunofluorescently-labeled images of the nuclear envelope (**Fig. S10**). The results indicates that multinucleates of MDA-MB-231 PACCs have a lower population of cells with mitotically catastrophic nuclei compared to PC3-PACCs at the early time points in the recovery period, whereas reversely increased as recovery time was prolonged. These findings may suggest that an active DDR suppresses multinucleation

due to mitotic catastrophe, preventing cell death.

To evaluate the effect of different treatments on multi- vs mononucleation in treated cells, PC3 cells were treated with with [LD50] doses of two additional chemotherapeutic drugs, etoposide and docetaxel, for 72 hours (**Fig. S11**). The proportion of multinucleates was significantly different between the two drugs and compared to cisplatin. The trend of increased mononucleate morphology at later recovery times was consistent with cisplatin treatment. Differences in the multinucleation level in the docetaxel treatment group are likely due to the mechanism of this therapy, which stabilizes microtubules to inhibit cell proliferation[107]. These results suggest that mononucleated PC3 cells will eventually become a dominant morphological phenotype in the longer recovery period.

Discussion

Insert short summary paragraph of your findings and link to the PACC state →
What you observed as cells surviving after therapy == PACC state. Introduce your summary cartoon here.

It has been recently appreciated that cancer cells in the PACC state are important players in tumor biology, specifically related to therapy resistance and cancer recurrence. Our group and others have shown that cancer cells access the PACC state via a polyploidization program in response to environmental stress, such as the genotoxic chemotherapies utilized in this study. The resulting enlargement of both nuclear and cell size is hypothesized to aid the cell in adapting to toxic environments such as therapeutic stress. Prior to this study, it was widely regarded that one key feature of cells in the PACC state is their multinucleated and/or multi-lobulated nuclei[35-37,108-111]. However, through 2D and 3D immunofluorescence microscopy, we demonstrated that not only do mononucleated PACCs exist, but that for cells that adopt the PACC state generated under cisplatin, docetaxel, and etoposide chemotherapy, mononucleates become the predominant cell type over the course of cellular recovery from therapy.

We show through live cell imaging of FUCCI-labeled cells and EdU experiments that cells in the PACC state engage in active DNA replication without entry into mitosis, a phenomenon known as endocycling. This provides a mechanistic explanation for the increase in nuclear size that we observed in this study and that others have observed in studies of similar large, polyploid cancer cells[26,35-37,110-113]. These data further our understanding of the functional characteristics of cancer cells in the PACC state. Cells in the PACC state are not simply cancer cells that are stalled at the G2/M DNA damage checkpoint in mitosis; rather, they bypass this checkpoint completely. Interestingly, while the percentage of cells that actively incorporating EdU decreased as a function of recovery time, indicating that the endocycling program accessed by the cells might be more important or relevant earlier in treatment recovery, cytoplasmic volumes steadily increased in a manner that suggests consistent biosynthesis of contents beyond genomic material.

The nucleolus plays a crucial role in nuclear homeostasis as an RNA production hub[74-77], and both the size and number of nucleoli are highly correlated with cancer malignancy and have previously been used as a diagnostic signature[80]. Interestingly, cells in the PACC state showed a distinct nucleolar phenotype, with fewer nucleoli of a larger size (**Fig. 4B, D**). This distinct pattern may be a consequence of endocycling, wherein the mitotic phase is completely bypassed, since the nucleolar structure disassembles at the mitotic phase and reassembles at interphase[74]. To the best of our knowledge, a distinct pattern of nucleolar size and number has not been reported in the cancer biology field, but it has been shown that stem cells often have fewer but larger nucleoli than differentiated somatic cells[114]. Other studies of large, polyploid cancer cells have suggested that these cells may act as a type of cancer stem cell, possessing stem cell-like features and cellular programs[23,26,31,33,35,37,48].Taken together with previous findings, our results suggest two functional consequences for PACC biology: mononucleated cells in the PACC state may be in a functionally dormant state (i.e., a nondividing yet active state) and that they may have a higher potential to differentiate into therapeutic-resistant progeny with a level of phenotypic plasticity due to similarities to stem cells.

A final focus of this paper was to characterize the extent to which DNA damage and the cellular response to this damage impact both the shift in nuclear morphology of treated cells, both those that eventually die and those that access the pro-survival PACC state. We observed that immediately after treatment, cells

display a high level of DNA damage, measured via staining of gh2ax. This was visible as gh2ax foci, representing sites of DDR machinery recruitment and DNA damage repair, as well as pan-stained nuclei, where the gh2ax is present at a consistent level throughout the entirety of the genome, representing excessive and widespread DNA damage that induces acute apoptosis[16,89,90]. We suggest that treated cells with pan-stained nuclei are non-viable and destined for death early in following therapy release, while cells with gh2ax foci are more likely have successful DNA damage repair and access the PACC state. However, counting gh2ax foci alone is not an optimal method to assess the level of DDR in the PACC state. To capture the level of DDR, we have newly defined the level of DDR in the PACC state by counting the colocalized gh2ax foci with 53BP1 foci and calculating the proportion of the colocalized gh2ax across recovery timepoints, since we hypothesized that the recruitment of DNA repair molecules is a key process of the DDR in the PACC state. 53BP1 (tumor suppressor P53-binding protein 1) localizes to sites of DNA damage and acts as a recruiter for the downstream effectors of DNA repair via the NHEJ pathway such as RIF1 and PTIP[85,115-117]. We observed that the colocalization of gh2ax and 53BP1 foci increased as a function of recovery time, indicating that the DDR seems to increase over time. Additionally, the relative death rate of treated cells (**Fig. 5B**) decreased over time. We hypothesize that the success of DNA repair is low initially but that it becomes more efficacious over time.

If cells are exposed to excessive genotoxic stress and the consequent DNA damage is overwhelming and essentially permanent, gh2ax expression displays a uniformly pan-stained pattern rather than foci formation[88-90]. Pan-stained gh2ax expression in nuclei also is indicative of early apoptotic cells. Treated cells initially had a pan-stained gh2ax pattern at a high rate (~50%), whereas the proportion of pan-stained nuclei in the population decreased in the recovering population (**Fig. S5**). The pan-stained 53BP1 pattern within nuclei was not observed in the treated population, and we surmise that this is also a feature of the PACC state nuclei since a distributed 53BP1 pattern is recognized as a failure of its recruitment to DNA damage sites[85,90,118-120].

Thus, the 53BP1 foci counts per area (**Fig. 5F)** can directly indicate the molecular level of 53BP1 in the PACC state, indicating that expression of this repair protein decreased at early time points of the recovery and returned to a similar level of untreated parental cells. The level of 53BP1 foci counts was correlated with the level of DDR (i.e., colocalization), supporting our hypothesis that 53BP1 recruitment is an important process for DDR in the PACC state. It is worthwhile to note that canonical HR pathway is active at S/G2 phase, whereas NHEJ pathway play a critical role in acute repair of DNA damage at all phases of a cell cycle[85,90,121-125]. The results of our DDR foci analysis (**Fig. 5D-G**) suggest that the NHEJ pathway is a primary mechanism of the DDR in the PACC state. Since the NHEJ pathway is error-prone DDR process even if it has a benefit for acute DNA damage repair, the HR pathway, which is an error-proof process, may be evolutionary selected as a main DDR pathway in a recovered population, and thus its role in cells in the PACC state will be worthwhile to examine in the future.

We observed that the level of apoptosis decreased in populations of treated cells over time in a pattern similar to the decrease in gh2ax pan-stained nuclei. Conversely, autophagy increased throughout cell recovery, suggesting that cells in the PACC state require a higher level of autophagy to maintain cellular homeostasis. It is also likely that that for some treated cells, this high level of autophagy, and more specifically nucleophagy, may play a role in cell death at later timepoints through the induction of autophagic cell death[97]. Together, our interrogation of DNA damage, apoptosis, and cell death present a paradigm where the early treated population contains a higher proportion of cells with a high level of widespread DNA damage that induces apoptosis, while with recovery, the treated population shifts toward a lower relative rate of cell death with some cells dying due to an overwhelming amount of autophagy secondary to DNA damage that was never resolved.

Both nuclei and cytoplasm volume were found to be higher in treated cells than treatment-naïve controls. The nuclear to cytoplasmic volume (NC) ratio has been regarded as a morphologic feature for the diagnosis of tumor malignancy: a higher NC ratio indicates high malignancy[62,64,126], while a low NC ratio is associated with the phenotypes of cell cycle arrest, replicative aging, senescence exhibiting lower cell function and proliferative potential, and lower RNA and protein concentrations[127]. Interestingly, while PC3 cells in the PACC state exhibited both phenotypes (having both high and low NC ratios), our findings indicate a overall lower NC ratio in the population of cells in the PACC state compared to parental cancer

cells, particularly at days 10 and 15 post-therapy. In the future, it will be worthwhile to investigate this novel hybrid phenotype to reveal its relevance to cancer recurrence.

Abnormal nuclear morphology has been regarded as a distinct phenotype of malignant cancer cells that facilitates invasion, migration, and metastasis[55,59,62,64]. Nuclear circularity is a representative 2D feature that allows for the evaluation of morphological abnormalities and it is used as a diagnostic parameter by pathologists[57,59,128,129]. Sphericity is a 3D version of circularity that may provide identical diagnostic potential or even better specificity due to the additional dimensional information[59,130,131]. Treated cells exhibited a decreasing nuclear volume as a function of recovery time, with the lowest sphericity values occurring in the population of cells in the PACC state at day 15. Since the deformability of nuclei is closely related to the invasion ability during the metastasis process[55,71,132], the recovered PACC population may exhibit a highly invasive morphological phenotype that facilitates cancer metastasis.

The life cycle of the PACC state has not yet been explored[31]. One characteristic of cells in the PACC state is dormancy[28,29,31,33,35]. Cells in the PACC state exist in a dormant state in terms of cell division and proliferation that prevents cell cycle arrest at mitotic checkpoints from genotoxic stress. This study, however, highlights that this dormancy phenotype is highly active, with evidence of repeated endocycling. Consequently, the presence of additional genomic material inside an enlarged nucleus may reinforce the genetic stability of these cells and enhance their resiliency against varied environmental stressors. It has been shown that a subset of cells in the PACC state eventually undergo some form of depolyploidization to generate resistant progeny and seed recurrences, ultimately contributing to cancer lethality[31,51,133]. It is possible that the extra genomic material of cells in the PACC state might also enhance the ability to give rise to variable offspring and increase the likelihood of generating a resistant clone[134]. Growing evidence into the role of the PACC states relevant to cancer lethality suggests that the PACC state is a “hallmark of lethal cancer”[31]; nonetheless, 1) the exact mechanisms of entry into the PACC state, 2) the physiological changes during the dormant state, and 3) the timing of and mechanisms utilized by cells in the PACC state to rapidly differentiate into therapeutic resistant cells remain unknown.

Ultimately, the findings presented in this study suggest to the PACC research field and to cancer pathology that mononucleated cells in the PACC state are critical players in of the development of resistance to therapies and to eventual cancer recurrence (**Fig. 1**). We aim to continue characterizing the cellular and molecular programs that cancer cells in this newly-defined state utilize to thwart treatments and contribute to cancer lethality.

Author contributions

Kim, C-J: conceptualization, methodology, investigation, writing (original draft), writing (review and editing), visualization. Gonye, ALK: conceptualization, methodology, investigation, writing (original draft), writing (review and editing), visualization. Truskowski, K: methodology, investigation. Lee, C-F: investigation. Pienta, KJ: conceptualization, writing (review and editing), funding acquisition. Amend, SR: conceptualization, writing (review and editing), funding acquisition.

Funding

Kim, C-J was supported by the Basic Science Research Program through the National Research Foundation of Korea funded by the Ministry of Education (2021R1A6A3A14043146). Pienta, KJ was supported by National Cancer Institute grants U54CA143803, CA163124, CA093900, and CA143055, and the Prostate Cancer Foundation. Amend, SR was supported by the US Department of Defense CDMRP/PCRP 367 (W81XWH-20-10353), the Patrick C. Walsh Prostate Cancer Research Fund, and the Prostate Cancer Foundation.

References

1 Burrell, R. A. & Swanton, C. Tumour heterogeneity and the evolution of polyclonal drug resistance. *Mol Oncol* **8**, 1095-1111, doi:10.1016/j.molonc.2014.06.005 (2014).

2 Mansoori, N. *et al.* Mycobacterium tuberculosis Complex Drug Resistance in a High Tuberculosis

Incidence Area from the WHO Eastern Mediterranean Region. *J Pharm Pharm Sci* **20**, 428-434, doi:10.18433/J3J64H (2017).

3 Aleksakhina, S. N., Kashyap, A. & Imyanitov, E. N. Mechanisms of acquired tumor drug resistance. *Biochim Biophys Acta Rev Cancer* **1872**, 188310, doi:10.1016/j.bbcan.2019.188310 (2019).

4 Gottesman, M. M., Fojo, T. & Bates, S. E. Multidrug resistance in cancer: role of ATP-dependent transporters. *Nature reviews. Cancer* **2**, 48-58, doi:10.1038/nrc706 (2002).

5 Shibue, T. & Weinberg, R. A. EMT, CSCs, and drug resistance: the mechanistic link and clinical implications. *Nat Rev Clin Oncol* **14**, 611-629, doi:10.1038/nrclinonc.2017.44 (2017).

6 Ganapathi, R. N. & Ganapathi, M. K. Mechanisms regulating resistance to inhibitors of topoisomerase II. *Frontiers in pharmacology* **4**, 89, doi:10.3389/fphar.2013.00089 (2013).

7 Chisholm, R. H., Lorenzi, T. & Clairambault, J. Cell population heterogeneity and evolution towards drug resistance in cancer: Biological and mathematical assessment, theoretical treatment optimisation. *Biochim Biophys Acta* **1860**, 2627-2645, doi:10.1016/j.bbagen.2016.06.009 (2016).

8 Nikolaou, M., Pavlopoulou, A., Georgakilas, A. G. & Kyrodimos, E. The challenge of drug resistance in cancer treatment: a current overview. *Clin Exp Metastasis* **35**, 309-318, doi:10.1007/s10585-018-9903-0 (2018).

9 Cree, I. A. & Charlton, P. Molecular chess? Hallmarks of anti-cancer drug resistance. *BMC Cancer* **17**, 10, doi:10.1186/s12885-016-2999-1 (2017).

10 Pienta, K. J., Partin, A. W. & Coffey, D. S. Cancer as a disease of DNA organization and dynamic cell structure. *Cancer Res* **49**, 2525-2532 (1989).

11 Du, F., Liu, H., Lu, Y., Zhao, X. & Fan, D. Epithelial-to-Mesenchymal Transition: Liaison between Cancer Metastasis and Drug Resistance. *Crit Rev Oncog* **22**, 275-282, doi:10.1615/CritRevOncog.2018024855 (2017).

12 Dagogo-Jack, I. & Shaw, A. T. Tumour heterogeneity and resistance to cancer therapies. *Nat Rev Clin Oncol* **15**, 81-94, doi:10.1038/nrclinonc.2017.166 (2018).

13 McGranahan, N. & Swanton, C. Clonal Heterogeneity and Tumor Evolution: Past, Present, and the Future. *Cell* **168**, 613-628, doi:10.1016/j.cell.2017.01.018 (2017).

14 Meacham, C. E. & Morrison, S. J. Tumour heterogeneity and cancer cell plasticity. *Nature* **501**, 328-337, doi:10.1038/nature12624 (2013).

15 Marusyk, A. & Polyak, K. Tumor heterogeneity: causes and consequences. *Biochim Biophys Acta* **1805**, 105-117, doi:10.1016/j.bbcan.2009.11.002 (2010).

16 Andor, N. *et al.* Pan-cancer analysis of the extent and consequences of intratumor heterogeneity. *Nat Med* **22**, 105-113, doi:10.1038/nm.3984 (2016).

17 Turajlic, S., Sottoriva, A., Graham, T. & Swanton, C. Resolving genetic heterogeneity in cancer. *Nat Rev Genet* **20**, 404-416, doi:10.1038/s41576-019-0114-6 (2019).

18 Caswell, D. R. & Swanton, C. The role of tumour heterogeneity and clonal cooperativity in metastasis, immune evasion and clinical outcome. *BMC Med* **15**, 133, doi:10.1186/s12916-017-0900-y (2017).

19 Greaves, M. & Maley, C. C. Clonal evolution in cancer. *Nature* **481**, 306-313, doi:10.1038/nature10762 (2012).

20 Gillies, R. J., Verduzco, D. & Gatenby, R. A. Evolutionary dynamics of carcinogenesis and why targeted therapy does not work. *Nature reviews. Cancer* **12**, 487-493, doi:10.1038/nrc3298 (2012).

21 Gatenby, R. & Brown, J. The Evolution and Ecology of Resistance in Cancer Therapy. *Cold Spring Harb Perspect Med* **8**, doi:10.1101/cshperspect.a033415 (2018).

22 Hanahan, D. & Weinberg, R. A. The hallmarks of cancer. *Cell* **100**, 57-70, doi:10.1016/s0092-8674(00)81683-9 (2000).

23 Kuczler, M. D., Olseen, A. M., Pienta, K. J. & Amend, S. R. ROS-induced cell cycle arrest as a mechanism of resistance in polyaneuploid cancer cells (PACCs). *Prog Biophys Mol Biol* **165**, 3-7, doi:10.1016/j.pbiomolbio.2021.05.002 (2021).

24 Kuczler, M. D., Olseen, A. M., Pienta, K. J. & Amend, S. R. ROS-induced cell cycle arrest as a mechanism of resistance in polyaneuploid cancer cells (PACCs). *Progress in Biophysics and Molecular Biology* **165**, 3-7, doi:https://doi.org/10.1016/j.pbiomolbio.2021.05.002 (2021).

25 Fox, D. T., Soltis, D. E., Soltis, P. S., Ashman, T.-L. & Van De Peer, Y. Polyploidy: A Biological Force From Cells to Ecosystems. *Trends in Cell Biology* **30**, 688-694, doi:10.1016/j.tcb.2020.06.006 (2020).

26 Amend, S. R. *et al.* Polyploid giant cancer cells: Unrecognized actuators of tumorigenesis, metastasis, and resistance. *The Prostate* **79**, 1489-1497, doi:10.1002/pros.23877 (2019).

27 Pienta, K. J., Hammarlund, E. U., Axelrod, R., Brown, J. S. & Amend, S. R. Poly-aneuploid cancer cells promote evolvability, generating lethal cancer. *Evolutionary Applications* **13**, 1626-1634, doi:10.1111/eva.12929 (2020).

28 Kostecka, L. G., Pienta, K. J. & Amend, S. R. Lipid droplet evolution gives insight into polyaneuploid cancer cell lipid droplet functions. *Medical Oncology* **38**, doi:10.1007/s12032-021-01584-w (2021).

29 Lin, K.-C. *et al.* An in vitro tumor swamp model of heterogeneous cellular and chemotherapeutic landscapes. *Lab on a Chip* **20**, 2453-2464, doi:10.1039/d0lc00131g (2020).

30 Kostecka, L. G. *et al.* High KIFC1 expression is associated with poor prognosis in prostate cancer. *Medical Oncology* **38**, doi:10.1007/s12032-021-01494-x (2021).

31 Pienta, K. J., Hammarlund, E. U., Brown, J. S., Amend, S. R. & Axelrod, R. M. Cancer recurrence and lethality are enabled by enhanced survival and reversible cell cycle arrest of polyaneuploid cells. *Proceedings of the National Academy of Sciences* **118**, e2020838118, doi:10.1073/pnas.2020838118 (2021).

32 Pienta, K. J. *et al.* Cancer cells employ an evolutionarily conserved polyploidization program to resist therapy. *Semin Cancer Biol*, doi:10.1016/j.semcancer.2020.11.016 (2020).

33 Mallin, M. M., Pienta, K. J. & Amend, S. R. Cancer cell foraging to explain bone-specific metastatic progression. *Bone*, 115788, doi:10.1016/j.bone.2020.115788 (2020).

34 Alharbi, A. M., De Marzo, A. M., Hicks, J. L., Lotan, T. L. & Epstein, J. I. Prostatic Adenocarcinoma With Focal Pleomorphic Giant Cell Features A Series of 30 Cases. *Am J Surg Pathol* **42**, 1286-1296, doi:10.1097/Pas.0000000000001112 (2018).

35 Mirzayans, R., Andrais, B. & Murray, D. Roles of Polyploid/Multinucleated Giant Cancer Cells in Metastasis and Disease Relapse Following Anticancer Treatment. *Cancers* **10**, 118, doi:10.3390/cancers10040118 (2018).

36 Illidge, T. POLYPLOID GIANT CELLS PROVIDE A SURVIVAL MECHANISM FOR p53 MUTANT CELLS AFTER DNA DAMAGE. *Cell Biology International* **24**, 621-633, doi:10.1006/cbir.2000.0557 (2000).

37 Chen, J. *et al.* Polyploid Giant Cancer Cells (PGCCs): The Evil Roots of Cancer. *Current Cancer Drug Targets* **19**, 360-367, doi:http://dx.doi.org/10.2174/1568009618666180703154233 (2019).

38 Martin, S. K. *et al.* Multinucleation and Mesenchymal-to-Epithelial Transition Alleviate Resistance to Combined Cabazitaxel and Antiandrogen Therapy in Advanced Prostate Cancer. *Cancer Research* **76**, 912-926, doi:10.1158/0008-5472.can-15-2078 (2016).

39 Wolberg, W. H., Nick Street, W. & Mangasarian, O. L. Importance of Nuclear Morphology in Breast Cancer Prognosis. *Clinical Cancer Research* **5**, 3542-3548 (1999).

40 Liu, J. The dualistic origin of human tumors. *Seminars in Cancer Biology* **53**, 1-16, doi:https://doi.org/10.1016/j.semcancer.2018.07.004 (2018).

41 Virchow, R. *et al. Cellular pathology as based upon physiological and pathological histology; twenty lectures delivered in the Pathological Institute of Berlin during the months of February, March, and April, 1858*. (John Churchill, 1860).

42 Lin, K.-C. *et al.* The role of heterogeneous environment and docetaxel gradient in the emergence of polyploid, mesenchymal and resistant prostate cancer cells. *Clinical & Experimental Metastasis* **36**, 97-108, doi:10.1007/s10585-019-09958-1 (2019).

43 Orr-Weaver, T. L. When bigger is better: the role of polyploidy in organogenesis. *Trends in Genetics* **31**, 307-315, doi:10.1016/j.tig.2015.03.011 (2015).

44 Pandit, S. K., Westendorp, B. & de Bruin, A. Physiological significance of polyploidization in mammalian cells. *Trends in Cell Biology* **23**, 556-566, doi:https://doi.org/10.1016/j.tcb.2013.06.002 (2013).

45 Van De Peer, Y., Maere, S. & Meyer, A. The evolutionary significance of ancient genome duplications. *Nature Reviews Genetics* **10**, 725-732, doi:10.1038/nrg2600 (2009).

46 Lee, H. O., Davidson, J. M. & Duronio, R. J. Endoreplication: polyploidy with purpose. *Genes & Development* **23**, 2461-2477, doi:10.1101/gad.1829209 (2009).

47 Comai, L. The advantages and disadvantages of being polyploid. *Nature Reviews Genetics* **6**, 836-846, doi:10.1038/nrg1711 (2005).

48 Pienta, K. J. *et al.* Cancer cells employ an evolutionarily conserved polyploidization program to resist therapy. *Seminars in Cancer Biology*, doi:10.1016/j.semcancer.2020.11.016 (2020).

49 Derks, W. & Bergmann, O. Polyploidy in Cardiomyocytes. *Circulation Research* **126**, 552-565, doi:10.1161/circresaha.119.315408 (2020).

50 Lens, S. M. A. & Medema, R. H. Cytokinesis defects and cancer. *Nature Reviews Cancer* **19**, 32-45, doi:10.1038/s41568-018-0084-6 (2019).

51 Vitale, I. *et al.* Illicit survival of cancer cells during polyploidization and depolyploidization. *Cell Death & Differentiation* **18**, 1403-1413, doi:10.1038/cdd.2010.145 (2011).

52 Gentric, G. & Desdouets, C. Polyploidization in Liver Tissue. *The American Journal of Pathology* **184**, 322-331, doi:https://doi.org/10.1016/j.ajpath.2013.06.035 (2014).

53 Gjelsvik, K. J., Besen-McNally, R. & Losick, V. P. Solving the Polyploid Mystery in Health and

Disease. *Trends in Genetics* **35**, 6-14, doi:https://doi.org/10.1016/j.tig.2018.10.005 (2019).

54 Webster, M., Witkin, K. L. & Cohen-Fix, O. Sizing up the nucleus: nuclear shape, size and nuclear-envelope assembly. *Journal of Cell Science* **122**, 1477-1486, doi:10.1242/jcs.037333 (2009).

55 Denais, C. & Lammerding, J. 435-470 (Springer New York, 2014).

56 Kumar, N. *et al.* Computer-extracted features of nuclear morphology in hematoxylin and eosin images distinguish <scp>s</scp> tage <scp>II</scp> and <scp>IV</scp> colon tumors. *The Journal of Pathology* **257**, 17-28, doi:10.1002/path.5864 (2022).

57 Sengupta, D. *et al.* A deep hybrid learning pipeline for accurate diagnosis of ovarian cancer based on nuclear morphology. *PLOS ONE* **17**, e0261181, doi:10.1371/journal.pone.0261181 (2022).

58 Damodaran, K., Crestani, M., Jokhun, D. S. & Shivashankar, G. V. Nuclear morphometrics and chromatin condensation patterns as disease biomarkers using a mobile microscope. *PLOS ONE* **14**, e0218757, doi:10.1371/journal.pone.0218757 (2019).

59 Janssen, A. F. J., Breusegem, S. Y. & Larrieu, D. Current Methods and Pipelines for Image-Based Quantitation of Nuclear Shape and Nuclear Envelope Abnormalities. *Cells* **11**, 347, doi:10.3390/cells11030347 (2022).

60 Mi, H. *et al.* Predictive models of response to neoadjuvant chemotherapy in muscle-invasive bladder cancer using nuclear morphology and tissue architecture. *Cell Reports Medicine* **2**, 100382, doi:10.1016/j.xcrm.2021.100382 (2021).

61 Hou, L. *et al.* Dataset of segmented nuclei in hematoxylin and eosin stained histopathology images of ten cancer types. *Scientific Data* **7**, doi:10.1038/s41597-020-0528-1 (2020).

62 Flores, L. F. *et al.* Nuclear Dynamics and Chromatin Structure: Implications for Pancreatic Cancer. *Cells* **10**, 2624, doi:10.3390/cells10102624 (2021).

63 Uhler, C. & Shivashankar, G. V. Nuclear Mechanopathology and Cancer Diagnosis. *Trends in Cancer* **4**, 320-331, doi:10.1016/j.trecan.2018.02.009 (2018).

64 Fischer, E. G. Nuclear Morphology and the Biology of Cancer Cells. *Acta Cytologica* **64**, 511-519, doi:10.1159/000508780 (2020).

65 Skinner, B. M. & Johnson, E. E. P. Nuclear morphologies: their diversity and functional relevance. *Chromosoma* **126**, 195-212, doi:10.1007/s00412-016-0614-5 (2017).

66 Koch, C. *et al.* Characterization of circulating breast cancer cells with tumorigenic and metastatic capacity. *EMBO Molecular Medicine* **12**, doi:10.15252/emmm.201911908 (2020).

67 Schindelin, J. *et al.* Fiji: an open-source platform for biological-image analysis. *Nat Methods* **9**, 676-682, doi:10.1038/nmeth.2019 (2012).

68 Stirling, D. R. *et al.* CellProfiler 4: improvements in speed, utility and usability. *BMC Bioinformatics* **22**, 433, doi:10.1186/s12859-021-04344-9 (2021).

69 Zambon, A. C. *et al.* Methods and sensors for functional genomic studies of cell-cycle transitions in single cells. *Physiol Genomics* **52**, 468-477, doi:10.1152/physiolgenomics.00065.2020 (2020).

70 Alisafaei, F., Jokhun, D. S., Shivashankar, G. V. & Shenoy, V. B. Regulation of nuclear architecture, mechanics, and nucleocytoplasmic shuttling of epigenetic factors by cell geometric constraints. *Proceedings of the National Academy of Sciences* **116**, 13200-13209, doi:10.1073/pnas.1902035116 (2019).

71 Fischer, T., Hayn, A. & Mierke, C. T. Effect of Nuclear Stiffness on Cell Mechanics and Migration of Human Breast Cancer Cells. *Frontiers in Cell and Developmental Biology* **8**, doi:10.3389/fcell.2020.00393 (2020).

72 Kidiyoor, G. R. *et al.* ATR is essential for preservation of cell mechanics and nuclear integrity during interstitial migration. *Nature Communications* **11**, doi:10.1038/s41467-020-18580-9 (2020).

73 Takaki, T. *et al.* Actomyosin drives cancer cell nuclear dysmorphia and threatens genome stability. *Nature Communications* **8**, 16013, doi:10.1038/ncomms16013 (2017).

74 Hernandez-Verdun, D. Assembly and disassembly of the nucleolus during the cell cycle. *Nucleus* **2**, 189-194, doi:10.4161/nucl.2.3.16246 (2011).

75 Caragine, C. M., Haley, S. C. & Zidovska, A. Nucleolar dynamics and interactions with nucleoplasm in living cells. *eLife* **8**, doi:10.7554/elife.47533 (2019).

76 Lafontaine, D. L. J., Riback, J. A., Bascetin, R. & Brangwynne, C. P. The nucleolus as a multiphase liquid condensate. *Nature Reviews Molecular Cell Biology* **22**, 165-182, doi:10.1038/s41580-020-0272-6 (2021).

77 Latonen, L. Phase-to-Phase With Nucleoli – Stress Responses, Protein Aggregation and Novel Roles of RNA. *Frontiers in Cellular Neuroscience* **13**, doi:10.3389/fncel.2019.00151 (2019).

78 Lafita-Navarro, M. C. & Conacci-Sorrell, M. Nucleolar stress: From development to cancer. *Semin Cell Dev Biol*, doi:10.1016/j.semcdb.2022.04.001 (2022).

79 Yang, K., Yang, J. & Yi, J. Nucleolar stress: Hallmarks, sensing mechanism and diseases. *Cell Stress* **2**, 125-140, doi:10.15698/cst2018.06.139 (2018).

80 Orsolic, I. *et al.* The relationship between the nucleolus and cancer: Current evidence and emerging paradigms. *Seminars in Cancer Biology* **37-38**, 36-50, doi:10.1016/j.semcancer.2015.12.004 (2016).

81 Diesch, J., Hannan, R. D. & Sanij, E. Perturbations at the ribosomal genes loci are at the centre of cellular dysfunction and human disease. *Cell & Bioscience* **4**, 43, doi:10.1186/2045-3701-4-43 (2014).

82 Polo, S. E. & Jackson, S. P. Dynamics of DNA damage response proteins at DNA breaks: a focus on protein modifications. *Genes & Development* **25**, 409-433, doi:10.1101/gad.2021311 (2011).

83 Pilié, P. G., Tang, C., Mills, G. B. & Yap, T. A. State-of-the-art strategies for targeting the DNA damage response in cancer. *Nature Reviews Clinical Oncology* **16**, 81-104, doi:10.1038/s41571-018-0114-z (2019).

84 Popp, H. D., Brendel, S., Hofmann, W.-K. & Fabarius, A. Immunofluorescence Microscopy of γH2AX and 53BP1 for Analyzing the Formation and Repair of DNA Double-strand Breaks. *Journal of Visualized Experiments*, doi:10.3791/56617 (2017).

85 Bártová, E., Legartová, S., Dundr, M. & Suchánková, J. A role of the 53BP1 protein in genome protection: structural and functional characteristics of 53BP1-dependent DNA repair. *Aging* **11**, 2488-2511, doi:10.18632/aging.101917 (2019).

86 <science.1076182.pdf>.

87 Moeglin, E. *et al.* Uniform Widespread Nuclear Phosphorylation of Histone H2AX Is an Indicator of Lethal DNA Replication Stress. *Cancers* **11**, 355, doi:10.3390/cancers11030355 (2019).

88 Meyer, B. *et al.* Clustered DNA damage induces pan-nuclear H2AX phosphorylation mediated by ATM and DNA–PK. *Nucleic Acids Research* **41**, 6109-6118, doi:10.1093/nar/gkt304 (2013).

89 Ding, D. *et al.* Induction and inhibition of the pan-nuclear gamma-H2AX response in resting human peripheral blood lymphocytes after X-ray irradiation. *Cell Death Discovery* **2**, 16011, doi:10.1038/cddiscovery.2016.11 (2016).

90 Feraudy, S. d., Revet, I., Bezrookove, V., Feeney, L. & Cleaver, J. E. A minority of foci or pan-nuclear apoptotic staining of γH2AX in the S phase after UV damage contain DNA double-strand breaks. *Proceedings of the National Academy of Sciences* **107**, 6870-6875, doi:doi:10.1073/pnas.1002175107 (2010).

91 Mathew, R., Karantza-Wadsworth, V. & White, E. Role of autophagy in cancer. *Nature Reviews Cancer* **7**, 961-967, doi:10.1038/nrc2254 (2007).

92 Koepke, L. *et al.* An improved method for high-throughput quantification of autophagy in mammalian cells. *Scientific Reports* **10**, doi:10.1038/s41598-020-68607-w (2020).

93 Kroemer, G. *et al.* Classification of cell death: recommendations of the Nomenclature Committee on Cell Death 2009. *Cell Death & Differentiation* **16**, 3-11, doi:10.1038/cdd.2008.150 (2009).

94 Yao, M. *et al.* Autophagy-Mediated Clearance of Free Genomic DNA in the Cytoplasm Protects the Growth and Survival of Cancer Cells. *Frontiers in Oncology* **11**, doi:10.3389/fonc.2021.667920 (2021).

95 Vera-Ramirez, L., Vodnala, S. K., Nini, R., Hunter, K. W. & Green, J. E. Autophagy promotes the survival of dormant breast cancer cells and metastatic tumour recurrence. *Nature Communications* **9**, doi:10.1038/s41467-018-04070-6 (2018).

96 Mathiassen, S. G., De Zio, D. & Cecconi, F. Autophagy and the Cell Cycle: A Complex Landscape. *Frontiers in Oncology* **7**, doi:10.3389/fonc.2017.00051 (2017).

97 Kroemer, G. & Levine, B. Autophagic cell death: the story of a misnomer. *Nat Rev Mol Cell Biol* **9**, 1004-1010, doi:10.1038/nrm2529 (2008).

98 Eliopoulos, A. G., Havaki, S. & Gorgoulis, V. G. DNA Damage Response and Autophagy: A Meaningful Partnership. *Frontiers in Genetics* **7**, doi:10.3389/fgene.2016.00204 (2016).

99 Papandreou, M.-E. & Tavernarakis, N. Nucleophagy: from homeostasis to disease. *Cell Death & Differentiation* **26**, 630-639, doi:10.1038/s41418-018-0266-5 (2019).

100 Jevtić, P., Edens, L. J., Vuković, L. D. & Levy, D. L. Sizing and shaping the nucleus: mechanisms and significance. *Current Opinion in Cell Biology* **28**, 16-27, doi:10.1016/j.ceb.2014.01.003 (2014).

101 Kumar, R. *et al.* Supraphysiologic Testosterone Induces Ferroptosis and Activates Immune Pathways through Nucleophagy in Prostate Cancer. *Cancer Research* **81**, 5948-5962, doi:10.1158/0008-5472.can-20-3607 (2021).

102 Zhang, D., Wang, Y. & Zhang, S. Asymmetric Cell Division in Polyploid Giant Cancer Cells and Low Eukaryotic Cells. *BioMed Research International* **2014**, 1-8, doi:10.1155/2014/432652 (2014).

103 Erenpreisa, J., Huna, A., Salmina, K., Jackson, T. R. & Cragg, M. S. Macroautophagy-aided elimination of chromatin. *Autophagy* **8**, 1877-1881, doi:10.4161/auto.21610 (2012).

104 Rajaraman, R., Rajaraman, M., Rajaraman, S. & Guernsey, D. Neosis – a paradigm of self-renewal in cancer. *Cell Biology International* **29**, 1084-1097, doi:10.1016/j.cellbi.2005.10.003 (2005).

105 Chen, J. *et al.* Polyploid Giant Cancer Cells (PGCCs): The Evil Roots of Cancer. *Curr Cancer Drug Targets* **19**, 360-367, doi:10.2174/1568009618666180703154233 (2019).

106 Puig, P.-E. *et al.* Tumor cells can escape DNA-damaging cisplatin through DNA endoreduplication and reversible polyploidy. *Cell Biology International* **32**, 1031-1043, doi:10.1016/j.cellbi.2008.04.021 (2008).

107 Mukhtar, E., Adhami, V. M. & Mukhtar, H. Targeting Microtubules by Natural Agents for Cancer Therapy. *Molecular Cancer Therapeutics* **13**, 275-284, doi:10.1158/1535-7163.mct-13-0791 (2014).

108 Erenpreisa, J. *et al.* Polyploid tumour cells elicit paradiploid progeny through depolyploidizing divisions and regulated autophagic degradation. *Cell Biol Int* **35**, 687-695, doi:10.1042/CBI20100762 (2011).

109 White-Gilbertson, S. & Voelkel-Johnson, C. Giants and monsters: Unexpected characters in the story of cancer recurrence. *Adv Cancer Res* **148**, 201-232, doi:10.1016/bs.acr.2020.03.001 (2020).

110 Zhang, D., Wang, Y. & Zhang, S. Asymmetric cell division in polyploid giant cancer cells and low eukaryotic cells. *Biomed Res Int* **2014**, 432652, doi:10.1155/2014/432652 (2014).

111 Zhang, Z. *et al.* Irradiation-induced polyploid giant cancer cells are involved in tumor cell repopulation via neosis. *Mol Oncol*, doi:10.1002/1878-0261.12913 (2021).

112 Mittal, K. *et al.* Multinucleated polyploidy drives resistance to Docetaxel chemotherapy in prostate cancer. *Br J Cancer* **116**, 1186-1194, doi:10.1038/bjc.2017.78 (2017).

113 Sundaram, M., Guernsey, D. L., Rajaraman, M. M. & Rajaraman, R. Neosis: a novel type of cell division in cancer. *Cancer Biol Ther* **3**, 207-218, doi:10.4161/cbt.3.2.663 (2004).

114 Gupta, S. & Santoro, R. Regulation and Roles of the Nucleolus in Embryonic Stem Cells: From Ribosome Biogenesis to Genome Organization. *Stem Cell Reports* **15**, 1206-1219, doi:10.1016/j.stemcr.2020.08.012 (2020).

115 FitzGerald, J. E., Grenon, M. & Lowndes, N. F. 53BP1: function and mechanisms of focal recruitment. *Biochem Soc Trans* **37**, 897-904, doi:10.1042/BST0370897 (2009).

116 Gupta, A. *et al.* Role of 53BP1 in the regulation of DNA double-strand break repair pathway choice. *Radiat Res* **181**, 1-8, doi:10.1667/RR13572.1 (2014).

117 Mirza-Aghazadeh-Attari, M. *et al.* 53BP1: A key player of DNA damage response with critical functions in cancer. *DNA Repair (Amst)* **73**, 110-119, doi:10.1016/j.dnarep.2018.11.008 (2019).

118 Schultz, L. B., Chehab, N. H., Malikzay, A. & Halazonetis, T. D. P53 Binding Protein 1 (53bp1) Is an Early Participant in the Cellular Response to DNA Double-Strand Breaks. *Journal of Cell Biology* **151**, 1381-1390, doi:10.1083/jcb.151.7.1381 (2000).

119 Panier, S. & Boulton, S. J. Double-strand break repair: 53BP1 comes into focus. *Nature Reviews Molecular Cell Biology* **15**, 7-18, doi:10.1038/nrm3719 (2014).

120 Zimmermann, M. & De Lange, T. 53BP1: pro choice in DNA repair. *Trends in Cell Biology* **24**, 108-117, doi:10.1016/j.tcb.2013.09.003 (2014).

121 Gupta, A. *et al.* Role of 53BP1 in the Regulation of DNA Double-Strand Break Repair Pathway Choice. *Radiation Research* **181**, 1-8, doi:10.1667/rr13572.1 (2014).

122 Löbrich, M. & Jeggo, P. A Process of Resection-Dependent Nonhomologous End Joining Involving the Goddess Artemis. *Trends in Biochemical Sciences* **42**, 690-701, doi:10.1016/j.tibs.2017.06.011

(2017).

123 Karanam, K., Loewer, A. & Lahav, G. Dynamics of the DNA damage response: insights from live-cell imaging. *Briefings in Functional Genomics* **12**, 109-117, doi:10.1093/bfgp/els059 (2013).

124 Yue, X., Bai, C., Xie, D., Ma, T. & Zhou, P.-K. DNA-PKcs: A Multi-Faceted Player in DNA Damage Response. *Frontiers in Genetics* **11**, doi:10.3389/fgene.2020.607428 (2020).

125 Krajewska, M., Fehrmann, R., de Vries, E. & van Vugt, M. Regulators of Homologous Recombination Repair as Novel Targets for Cancer Treatment. *Frontiers in Genetics* **6**, doi:10.3389/fgene.2015.00096 (2015).

126 Nandakumar, V. *et al.* Isotropic 3D Nuclear Morphometry of Normal, Fibrocystic and Malignant Breast Epithelial Cells Reveals New Structural Alterations. **7**, e29230, doi:10.1371/journal.pone.0029230 (2012).

127 Neurohr, G. E. *et al.* Excessive Cell Growth Causes Cytoplasm Dilution And Contributes to Senescence. *Cell* **176**, 1083-1097.e1018, doi:10.1016/j.cell.2019.01.018 (2019).

128 Huang, H. *et al.* Cancer diagnosis by nuclear morphometry using spatial information. *Pattern Recognition Letters* **42**, 115-121, doi:10.1016/j.patrec.2014.02.008 (2014).

129 Schöchlin, M. *et al.* A nuclear circularity-based classifier for diagnostic distinction of desmoplastic from spindle cell melanoma in digitized histological images. *J Pathol Inform* **5**, 40-40, doi:10.4103/2153-3539.143335 (2014).

130 Coyne, A. N. & Rothstein, J. D. Nuclear lamina invaginations are not a pathological feature of C9orf72 ALS/FTD. *Acta Neuropathologica Communications* **9**, doi:10.1186/s40478-021-01150-5 (2021).

131 Goswami, R. *et al.* Mechanical Shielding in Plant Nuclei. *Current Biology* **30**, 2013-2025.e2013, doi:10.1016/j.cub.2020.03.059 (2020).

132 Bell, E. S. & Lammerding, J. Causes and consequences of nuclear envelope alterations in tumour progression. *European Journal of Cell Biology* **95**, 449-464, doi:10.1016/j.ejcb.2016.06.007 (2016).

133 Verena Rohnalter, K. R., Florian Finkernagel, Till Adhikary, Julia Obert, Kristina Dorzweiler, Maike Bensberg, Sabine Muller-Brusselbach, Rolf Muller. A multi-stage process including transient polyploidization and EMT precedes the emergence of chemoresistent ovarian carcinoma cells with a dedifferentiated and pro-inflammatory secretory phenotype. *Oncotarget* **6**, 21 (2015).

134 Heng, J. & Heng, H. H. Two-phased evolution: Genome chaos-mediated information creation and maintenance. *Prog Biophys Mol Biol* **165**, 29-42, doi:10.1016/j.pbiomolbio.2021.04.003 (2021).

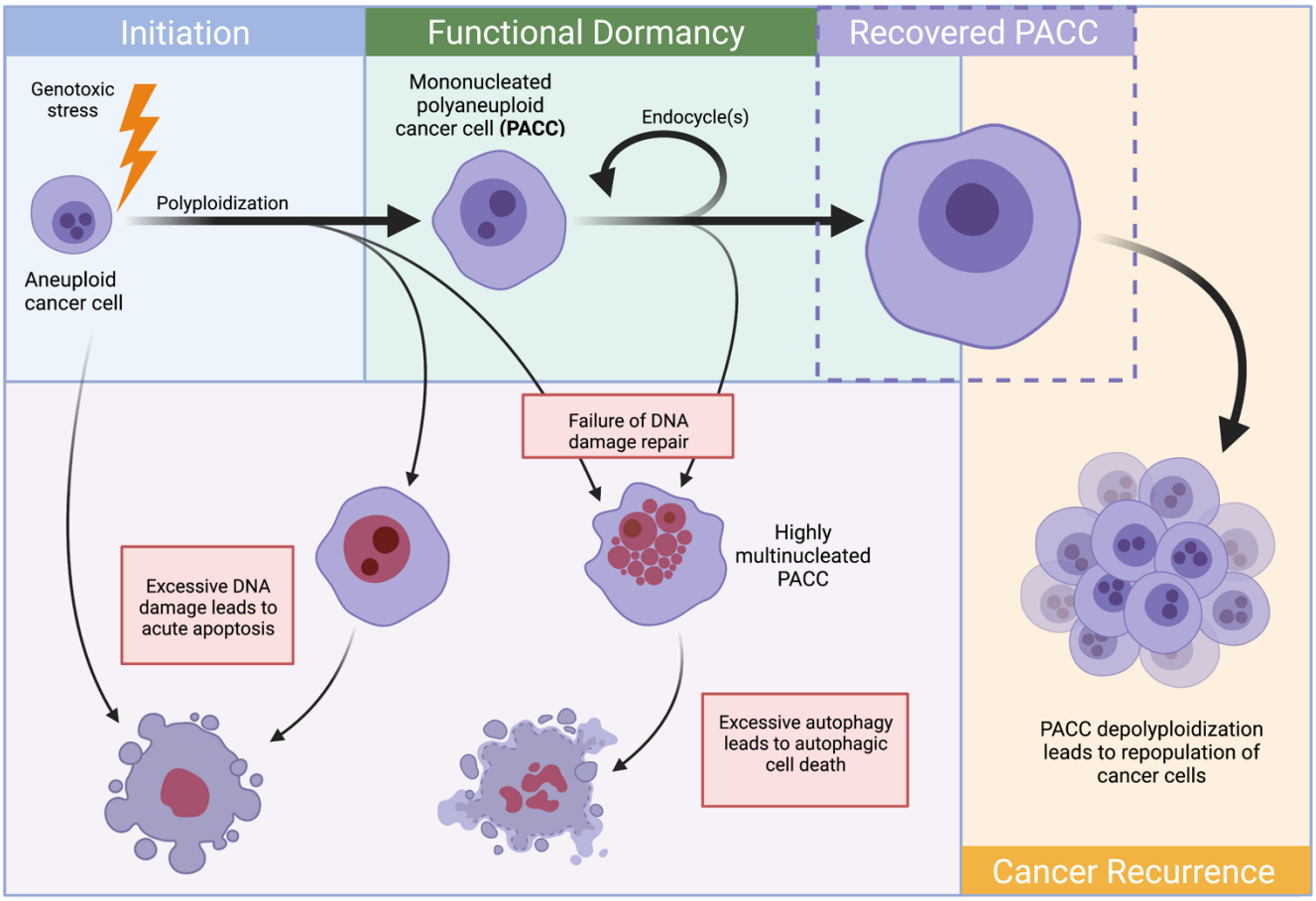

Figure 1. Schematic illustration of the proposed polyaneuploid cancer cell (PACC) life cycle. Initially, an aneuploid cancer cell experiences a temporary genotoxic stress. This can result in multiple trajectories: excessive DNA damage can occur before polyploidization, causing apoptosis; the cancer cell can undergo whole-genome duplication to become polyaneuploid, but then still have accumulated a burden of DNA damage high enough to lead to acute apoptosis; similarly, this polyaneuploid cell can attempt to repair its damaged genome but ultimately fail, becoming highly multinucleated and dying; lastly, it can undergo whole-genome duplication and become a viable mononucleated *polyaneuploid cancer cell (PACC)*. This PACC begins its period of functional dormancy, characterized by increases in cellular and nuclear volume that can be attributed to one or more endocycles. Not all PACCs survive until the end of this functional dormancy period: a sub-population will further try to repair DNA damage and also will experience heightened levels of autophagy as they try to achieve cellular homeostasis, ultimately leading to autophagic cell death. Eventually, after a period of time removed from the stressor, the recovered PACC state is reached. This PACC is capable of eventual depolyploidization that results in the revival of the aneuploid cancer cell population.

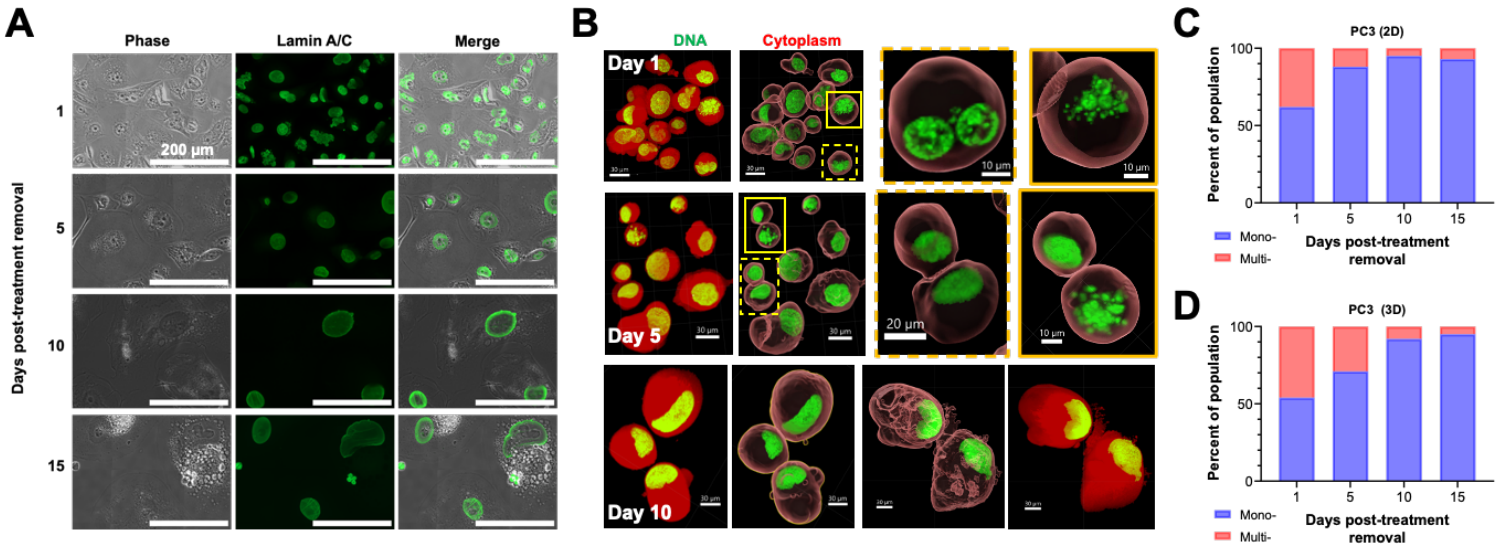

Figure 2. Characterization of the nuclear morphology of cisplatin-treated prostate cancer cells. Representative immunofluorescence images **(A)** to demonstrate the nuclear morphology of treated PC3 cells generated with 72h [LD50] cisplatin treatment following removal from chemotherapy. **(B)** Live treated PC3 cells at various timepoints in recovery were suspended in Matrigel and staining DNA with Vybrant™ DyeCycle™ Green Stain (for DNA) and CellTracker™ Orange (for cytoplasm). 3D images were obtained via confocal microscopy and images were rendered and volumes determined using Imaris 9.8 software. **(C)** Population distribution of mononucleated and multinucleated PC3s, derived from images described in (A). Nuclear morphology (mononucleated vs. multinucleated) was manually discriminated and counted using Fiji. At least 250 cells were analyzed per condition. **(D)** Nuclear morphology was also determined using the 3D imaging described in (B).

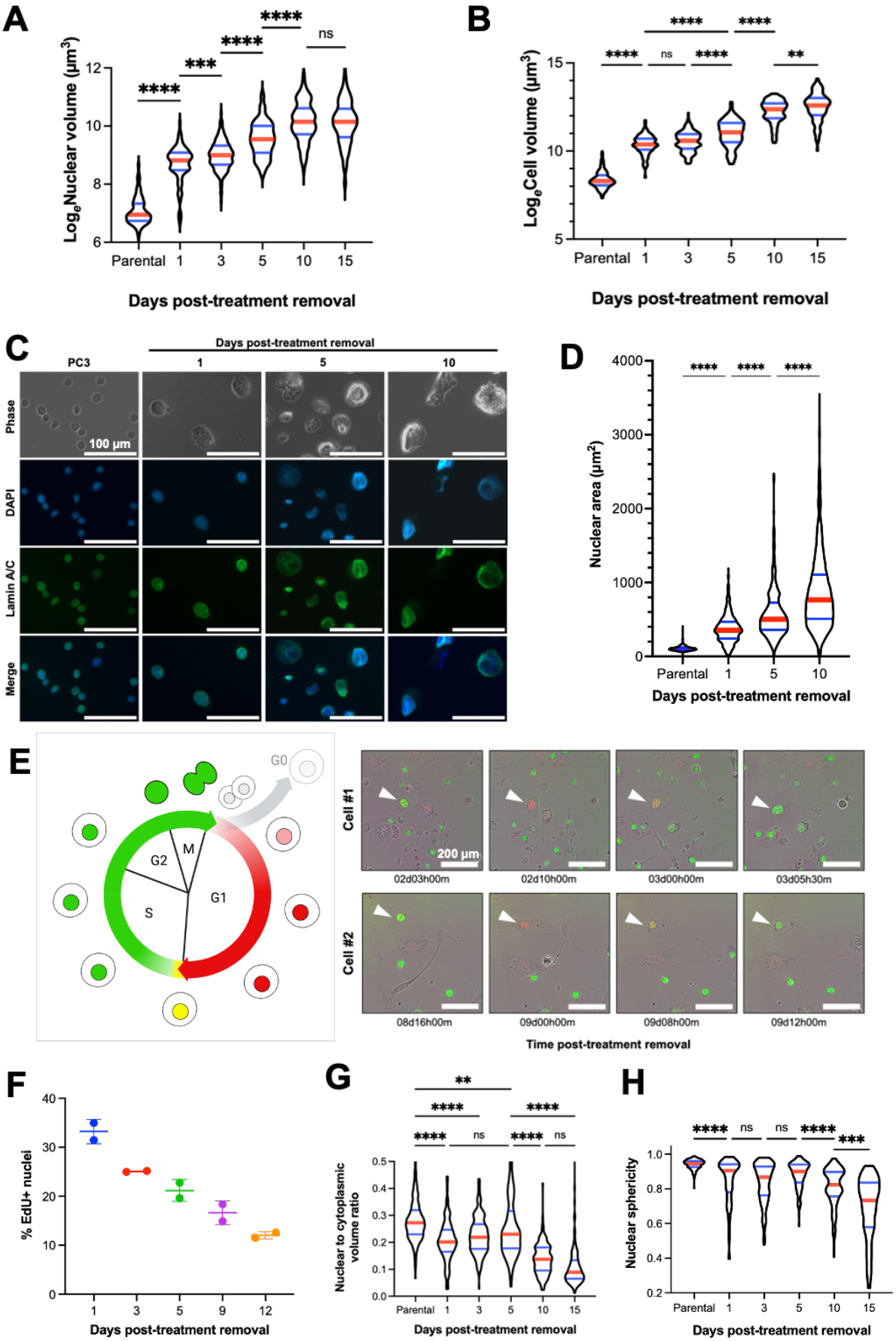
A
Log$_e$Nuclear volume (µm^3)
Days post-treatment removal
Parental
B
Log$_e$Cell volume (µm^3)
C
PC3
Days post-treatment removal
Phase
DAPI
Lamin A/C
Merge
100 µm
D
Nuclear area (µm^2)
E
G0
G2
M
S
G1
Cell #1
Cell #2
200 µm
02d03h00m
02d10h00m
03d00h00m
03d05h30m
08d16h00m
09d00h00m
09d08h00m
09d12h00m
Time post-treatment removal
F
% EdU+ nuclei
G
Nuclear to cytoplasmic volume ratio
H
Nuclear sphericity

Figure 3. Characterization of treated cancer cell nuclear size. Natural log-transformed **(A)** nuclear volume and **(B)** cellular volume of live treated PC3 cells, generated with 72h [LD50] cisplatin treatment, at various timepoints in recovery was determined by suspending cells in Matrigel and staining DNA with Vybrant™ DyeCycle™ Green Stain (for DNA) and CellTracker™ Orange (for cytoplasm). 3D images were obtained via confocal microscopy and images were rendered from volumetric determination using Imaris 9.8 software. Data was analyzed for differences between groups using a one-way ANOVA, a post-hoc Tukey's multiple comparisons tests was used to detect between-group differences. **(C)** Nuclei were isolated from parental and treated PC3 cells before mounting on PLL-coated dishes. Nuclei were stained for lamin A/C and covered with ProLong™ Diamond Antifade Mountant with DAPI before imaging on a Zeiss Observer Z1 microscope. The size of isolated nuclei was quantitated **(D)** via a custom CellProfiler 4.0 pipeline. A Kruskal-Wallis test was used to analyze if there were any significant differences among the samples, Dunn's multiple comparison's test used to test for comparisons between groups. To look for evidence of endocycling, PC3 cells were transduced with a FUCCI reporter, PC3-PACCs were generated from this reporter cell line, and timelapse microscopy **(E)** was performed with an Incucyte SX5 with images taken every 30min. Two representative cells are shown. **(F)** PC3-PACCs were tested for *de novo* DNA synthesis via a Click-It Plus EdU assay according to the manufacturer's protocol. Images were acquired using the 10x objective on a Zeiss Observer Z1 microscope. A custom CellProfiler pipeline was developed and used to quantify DAPI+Edu+ nuclei. **(G)** Nuclear and cytoplasmic volumes were used to calculate a nuclear to cytoplasmic volume ratio of treated PC3s at various timepoints past treatment removal. A Kruskal-Wallis test was used to analyze if there were any significant differences among the samples, Dunn's multiple comparison's test used to test for comparisons between groups. From the 3D nuclear imaging and rendering in Imaris, nuclear sphericity **(H)** was determined. A Kruskal-Wallis test was used to analyze if there were any significant differences among the samples, with a Dunn's multiple comparison's post-hoc test. For all statistical tests: * = $p<0.05$, ** = $p<0.01$, *** = $p<0.001$, **** = $p<0.0001$.

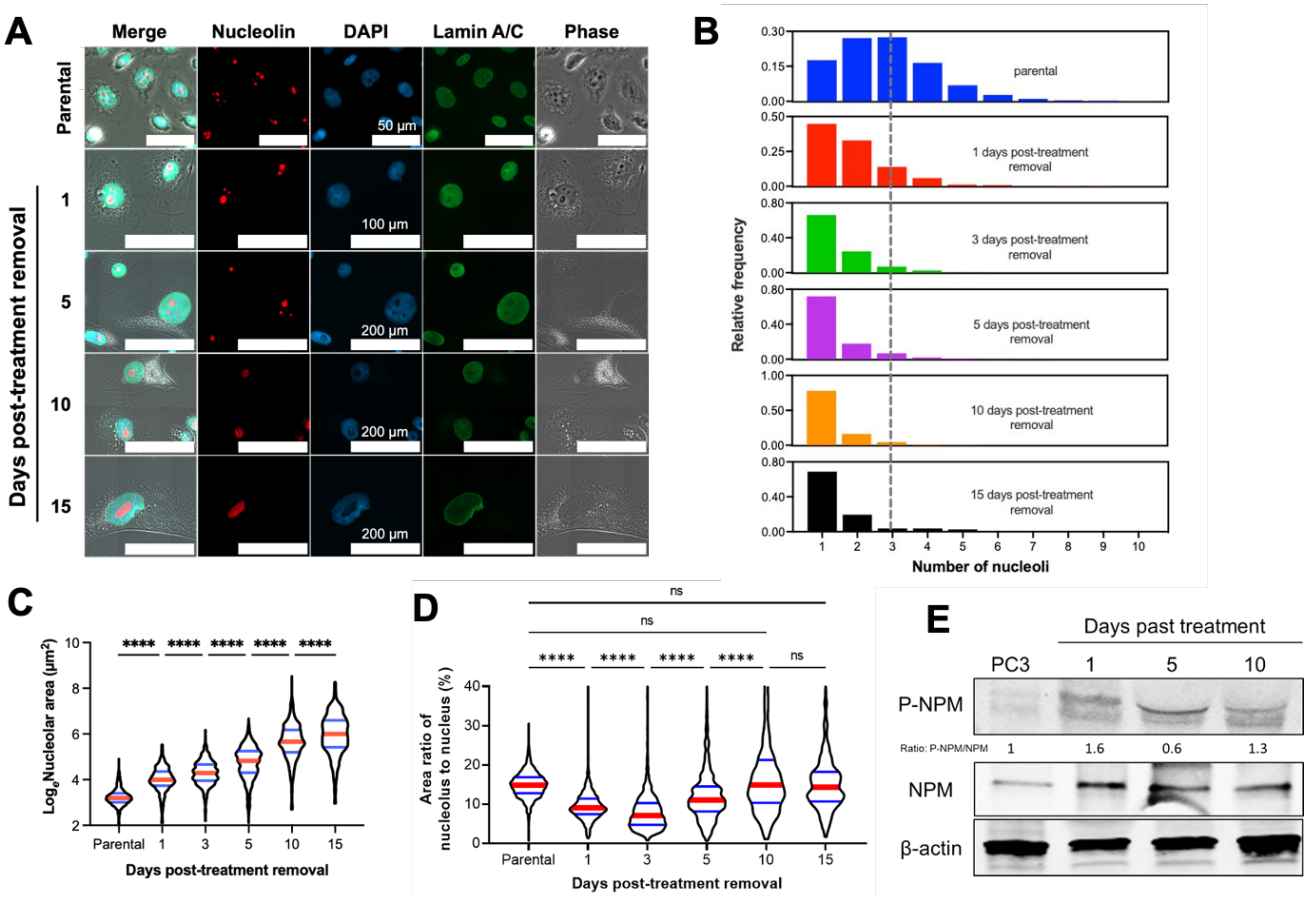

Figure 4. Nucleolar counts, size, and molecular signatures. Treated PC3 cancer cells generated with 72h [LD50] cisplatin treatment were stained for lamin A/C and nucleolin and were mounted with DAPI, **(A)** representative images of nucleoli are shown. A custom CellProfiler 4.0 pipeline was used to then determine the **(B)** number and **(C)** area of the nucleoli of the treated PC3s throughout the recovery period to become PACCs. Nucleolar area was analyzed for differences between groups using a one-way ANOVA, and a post-hoc Tukey's multiple comparisons test was used to detect between-group differences. The lamin A/C stain was used to calculate nuclear area, and thus **(D)** the nucleolar to nuclear area ratio at each timepoint post-treatment removal could be calculated; a Kruskal-Wallis test was used to analyze if there were any significant differences among the samples, with a Dunn's multiple comparison's post-hoc test. For all statistical tests: * = $p<0.05$, ** = $p<0.01$, *** = $p<0.001$, **** = $p<0.0001$.

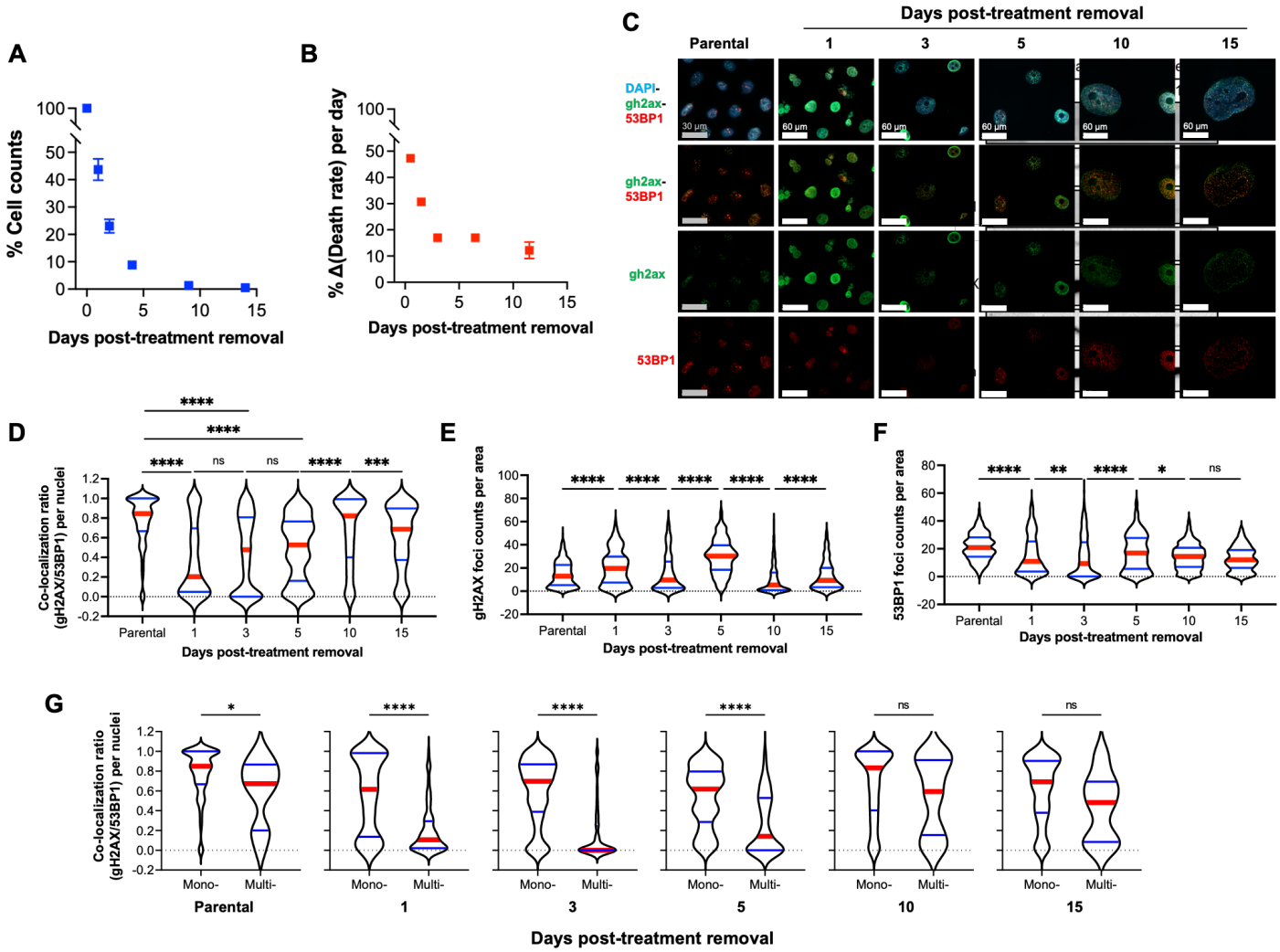

Figure 5. The DNA damage response in cisplatin-treated prostate cancer cells. Relative cell number (percent normalized to population count at 0 days post-treatment removal) as a function of recovery time **(A)** was determined for treated PC3 cells generated with 72h [LD50] cisplatin treatment. From this data, we also determined **(B)** the percent change in the death rate for each of the recovery days we investigated. **(C)** Immunofluorescence staining and imaging was used to visualize genomic contents (DAPI), sites of DNA damage (gH2AX), and DDR machinery recruitment (53BP1). From these images, a custom CellProfiler 4.0 pipeline was used to determine **(D)** the colocalization ratio of gH2AX with 53BP1, as well as a raw count per unit cellular area of the number of **(E)** gH2AX foci and **(F)** 53BP1 foci. For each day post-treatment recovery, were classified as mononucleates and multinucleates, and **(G)** the colocalization ratio of gH2AX with 53BP1 was determined for each cell class. Mann-Whitney tests were used to detect differences between groups in (D) through (G). For all statistical tests: * = p<0.05, ** = p<0.01, *** = p<0.001, **** = p<0.0001.

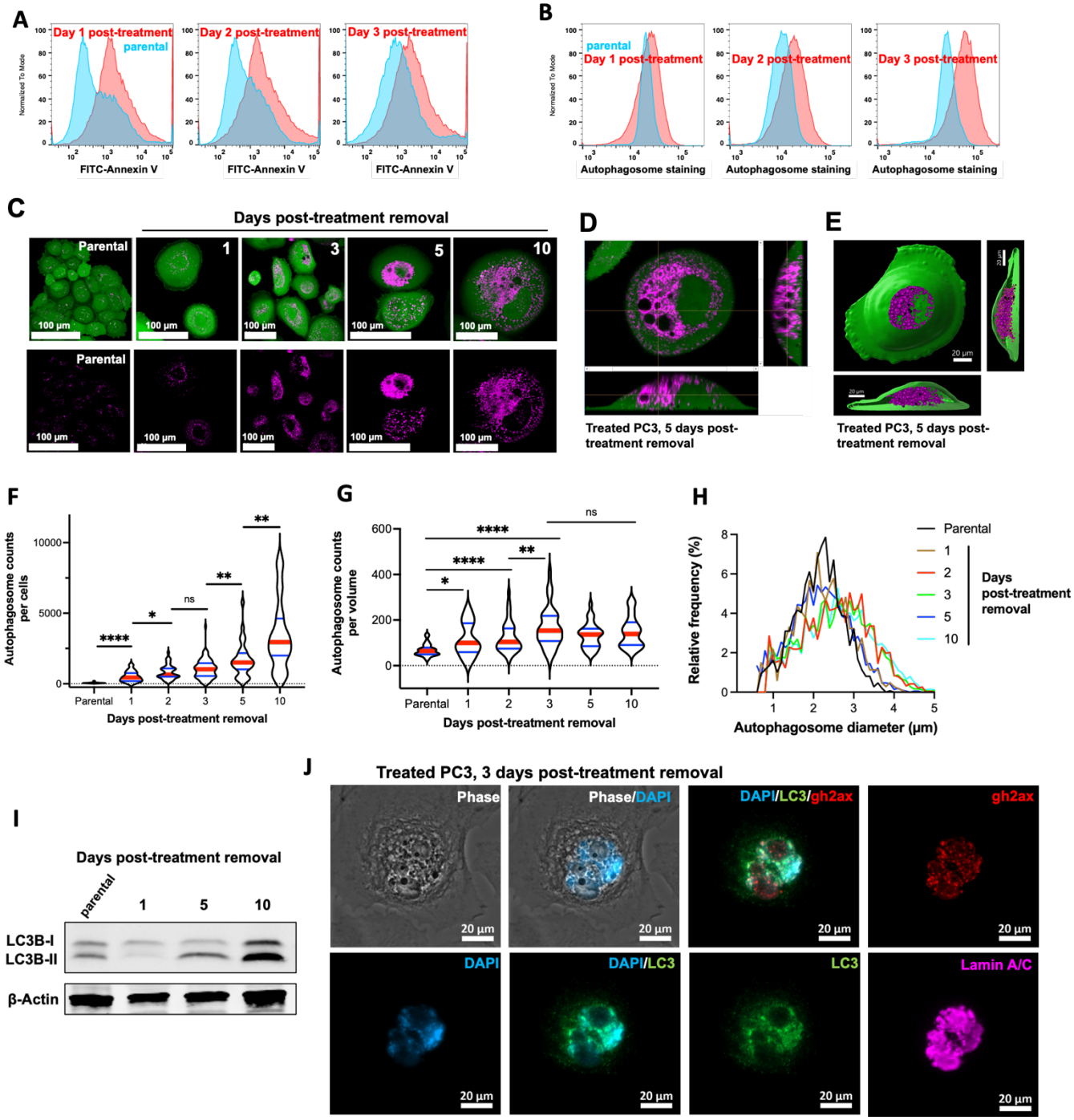

Figure 6. Treated prostate cancer cell death: apoptosis and autophagy. Flow cytometry was used to measure **(A)** surface expression of annexin V as a marker of apoptosis and **(B)** staining of autophagosomes (via Abcam's Autophagy Assay kit) in treated PC3s generated with 72h [LD50] cisplatin treatment at days 1, 2, and 3 post-treatment removal (PACC1, PACC2, and PACC3, respectively) compared to parental PC3 prostate cancer cells. The cytoplasm of live treated PC3s was labeled with Calcein AM, and the Autophagy Assay kit was similarly used to fluorescently label autophagosomes/autolysosomes for **(C)** 2D and **(D)** 3D imaging (pink = autophagic vesicles, green = cytoplasm). Additionally, **(E)** 3D images were rendered using Imaris 9.8 and **(F)** per cell autophagic vesicle counts were determined. **(G)** these counts were also normalized to cellular volume. Mann-Whitney tests were used to detect differences between groups in (F) and (G). **(H)** Imaris was also used to measure the diameter of individual autophagosomes at the different recovery days investigated in this experiment. Western blotting **(I)** was used to examine the expression of the autophagy-related proteins LC3B-I and LC3B-II over PC3-PACC recovery. **(J)** Immunofluorescent microscopy was also used to examine PC3-PACCs for colocalization of DAPI, gH2AX, and LC3 as evidence of nucleophagy. For all statistical tests: * = $p<0.05$, ** = $p<0.01$, *** = $p<0.001$, **** = $p<0.0001$.

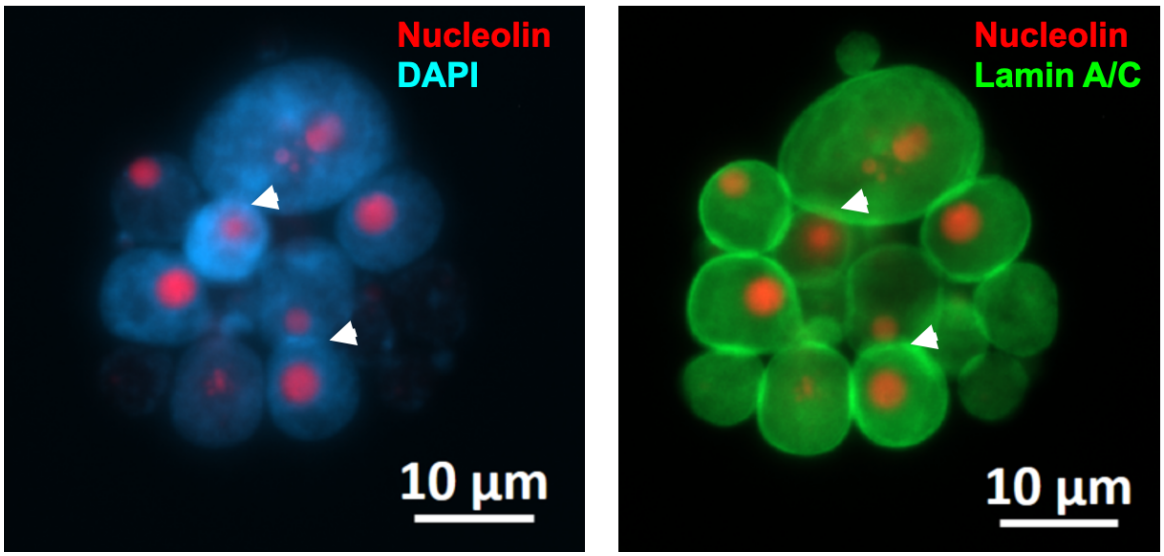

Figure S1. Differences in nuclear visualization between DAPI and lamin A/C. A cisplatin-treated PC3 cancer cell 1 day post-treatment removal was stained for nucleolin and lamin A/C and mounted with DAPI prior to immunofluorescent imaging. Differences in the ability of DAPI vs. lamin A/C to discriminate individual nuclei should be noted.

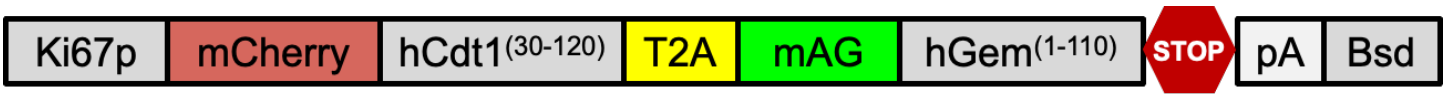

Figure S2. Ki67p-T2A-FUCCI construct. Gifted from Alexander Zambon.

Rendered nuclei in PC3-PACCs, 15 days post-treatment removal, with sphericity metric indicated.

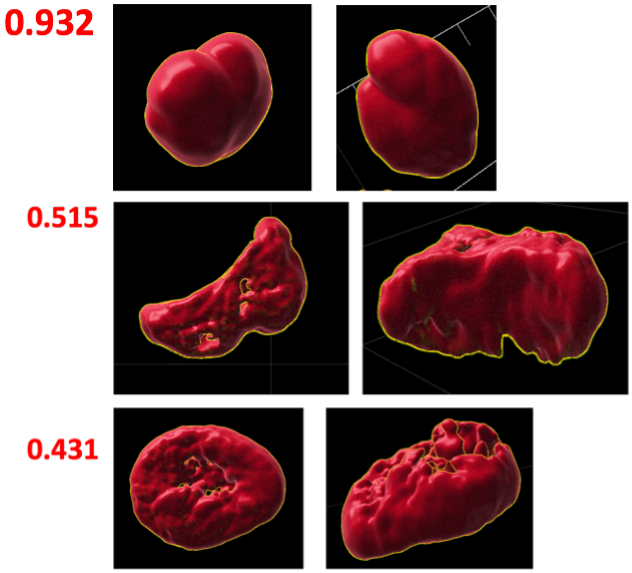

Figure S3. Visual reference for differences in sphericity. Live recovered PACCs 15 days post-treatment removal were stained with 10 μM Vybrant™ DyeCycle™ Green Stain. 3D confocal images were acquired and nuclear shapes were rendered in Imaris 9.8 prior to sphericity calculations.

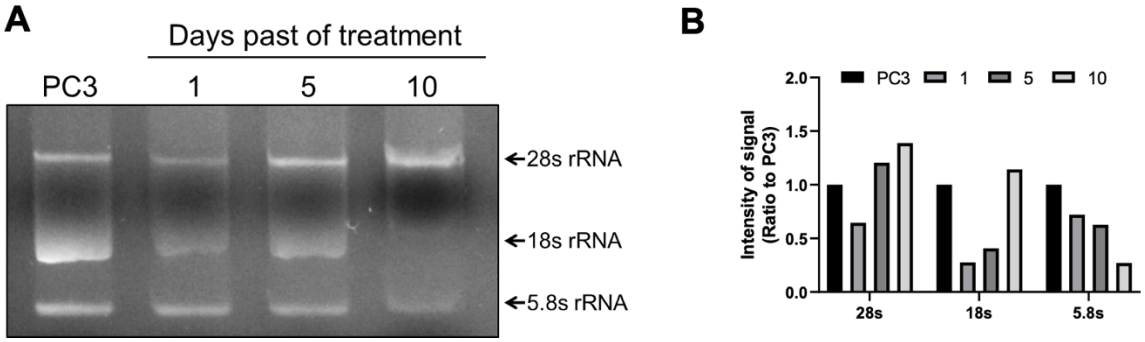

Figure S4. The rRNA pattern in parental PC3s and treated PC3s. PC3 prostate cancer cells were induced with 72h [LD50] cisplatin treatment. Total RNA was isolated and resolved via gel electrophoresis. Bands (28s, 18s, 5.8s) were visualized with EtBr staining.

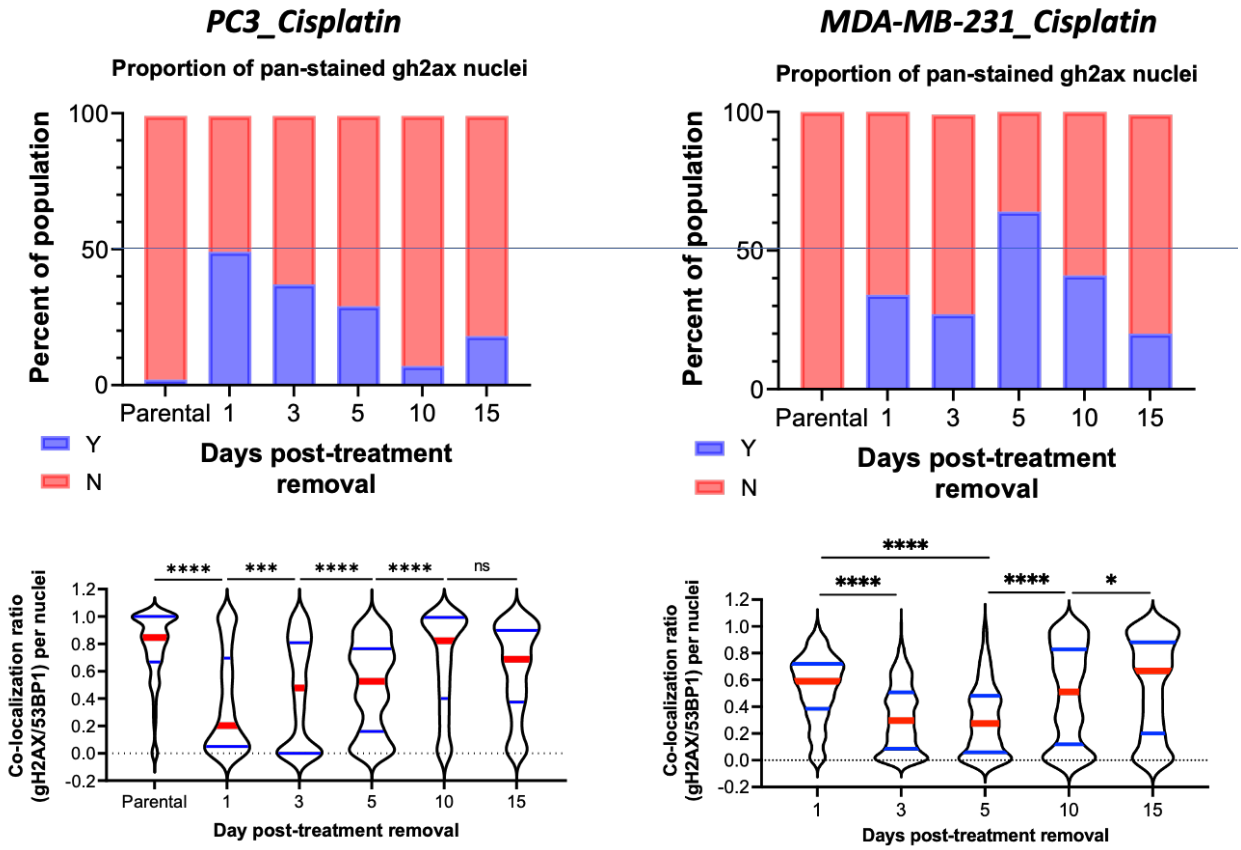

Figure S5. Pan-staining of gH2AX and gH2AX/53BP1 colocalization in cisplatin-treated PC3 prostate cancer cells vs. MDA-MB-231 breast cancer cells. Top graphs show the relative proportion of cells with (Y) and without (N) gH2AX pan-stained nuclei from analyze immunofluorescent microscopy images. Bottom graphs show the colocalization ratio of gH2AX with 53BP1; Mann-Whitney tests were used to detect differences between groups in (D) through (G). For all statistical tests: * = p<0.05, ** = p<0.01, *** = p<0.001, **** = p<0.0001.

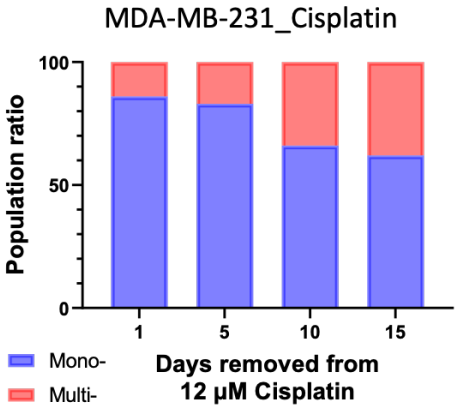

Figure S6. Characterization of treated MDA-MB-231 nuclear morphology. Population distribution of mononucleated and multinucleated treated MDA-MB-231s generated with 72h [LD50] cisplatin treatment, derived from immunofluorescent images of cells stained for lamin A/C and mounted with DAPI. Nuclear morphology (mononucleated vs. multinucleated) was manually discriminated and counted using Fiji software.

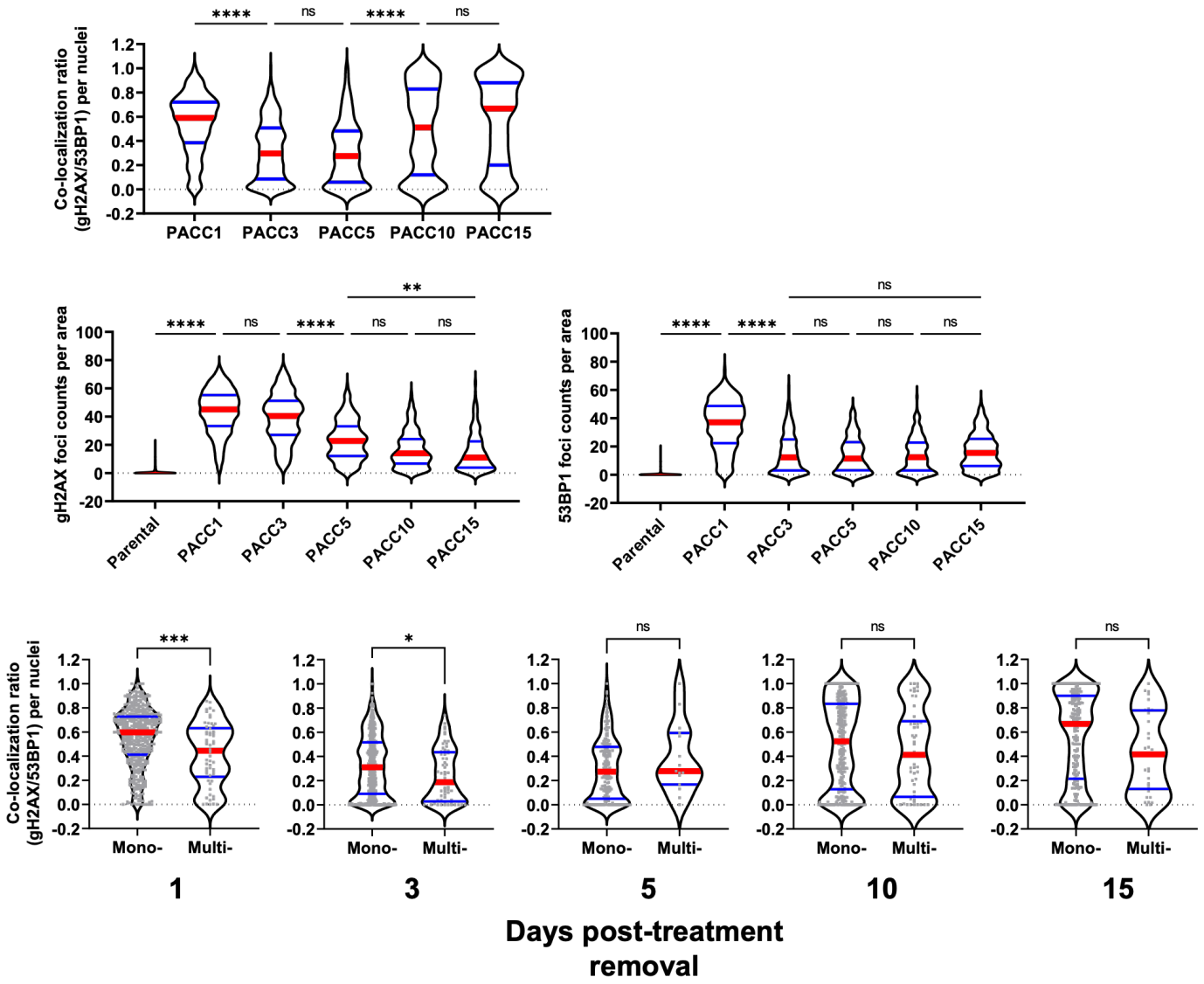

Figure S7. DDR foci analysis in treated MDA-MB-231 breast cancer cells. Similarly to Fig. 5, MDA-PACCs were generated with 72h [LD50] cisplatin treatment and immunofluorescence staining/imaging was used to visualize genomic contents (DAPI), sites of DNA damage (gH2AX), and DDR machinery recruitment (53BP1). Again, a custom CellProfiler 4.0 pipeline was used to determine the colocalization ratio of gH2AX with 53BP1, as well as a raw count per unit cellular area of the number of gH2AX foci and 53BP1 foci. For each day post-treatment recovery, were classified as mononucleates and multinucleates, and the colocalization ratio of gH2AX with 53BP1 was determined for each cell class. Mann-Whitney tests were used to detect differences between groups in (D) through (G). For all statistical tests: * = $p<0.05$, ** = $p<0.01$, *** = $p<0.001$, **** = $p<0.0001$.

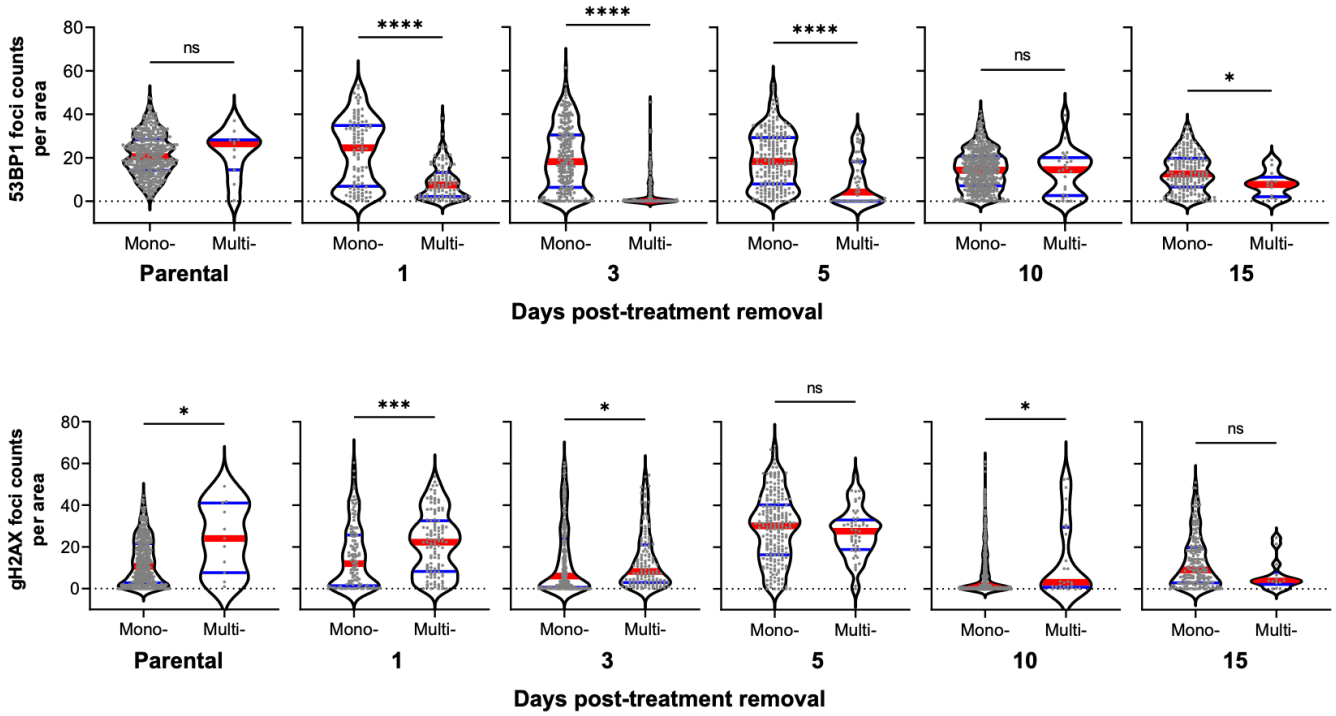

Figure S8. DDR foci counts in mononucleated vs. multinucleated treated MDA-MB-231s. Treated MDA-MB-231 cells were generated with 72h [LD50] cisplatin treatment and immunofluorescence staining/imaging was used to visualize genomic contents (DAPI), sites of DNA damage (gH2AX), and DDR machinery recruitment (53BP1). As a follow-up to Fig. S6, raw counts per unit cellular area of the number of gH2AX foci and 53BP1 foci were determined for mononucleate vs. multinucleate PACCs.

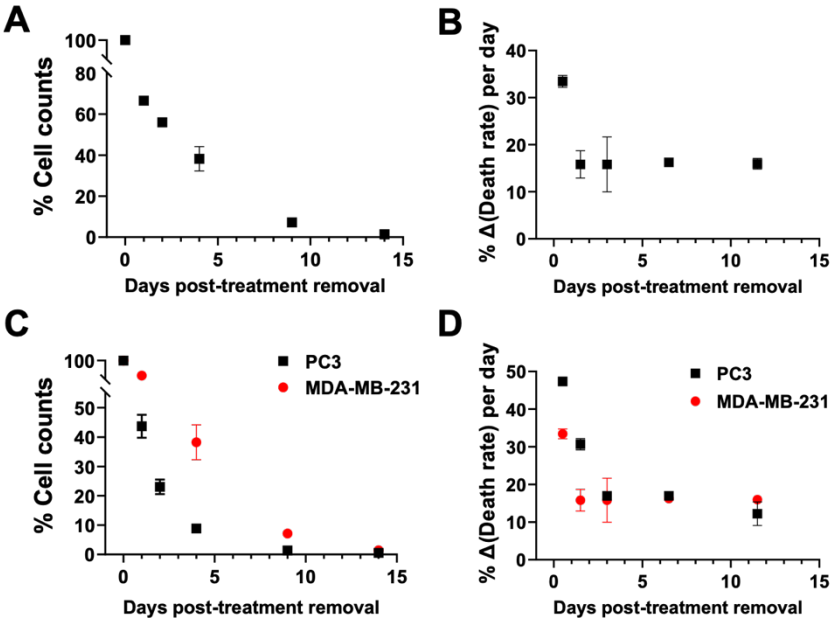

Figure S9. Differences in survival between treated PC3s and treated MDA-MB-231s. Relative cell number (percent normalized to population count at 0 days post-treatment removal) as a function of recovery time **(A)** was determined for treated MDA-MB-231s and treated PC3s generated with 72h [LD50] cisplatin treatment. From this data, we also determined **(B)** the percent change in the death rate for each of the recovery days we investigated. **(C)** and **(D)** show the comparison of both metrics between the PC3s and MDA-MB-231 cells.

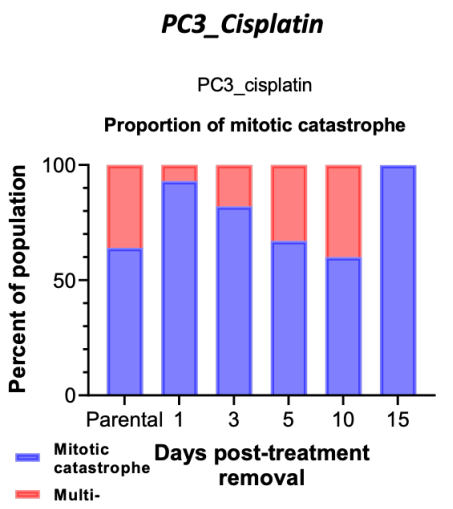

Nuclei counts	Mono	Multi except mitotic catastroph	Mitotic catastrophe
Parental	411	11	7
PACC1	100	110	102
PACC3	243	130	106
PACC5	205	48	32
PACC10	524	25	15
PACC15	183	13	13

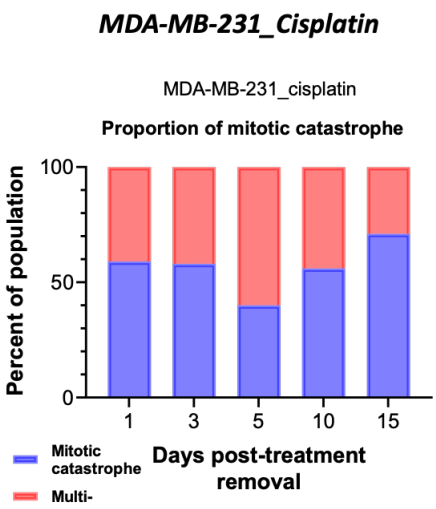

Nuclei counts	Mono	Multi except mitotic catastroph	Mitotic catastrophic
PACC1	527	58	34
PACC3	554	64	37
PACC5	187	15	6
PACC10	291	50	28
PACC15	253	34	24

Figure S10. Proportion of mitotic catastrophe in multinucleated cisplatin-treated PC3s and MDA-MB-231s. Treated PC3s and MDA-MB-231s were generated with 72h [LD50] cisplatin treatment and stained for lamin A/C and mounted with DAPI. Mononucleated, multinucleated, and mitotically catastrophic cells were classified via a custom CellProfiler 4.0 pipeline, and the proportion of multinucleated cells to those experiencing mitotic catastrophe were plotted across the different days post-treatment removal.

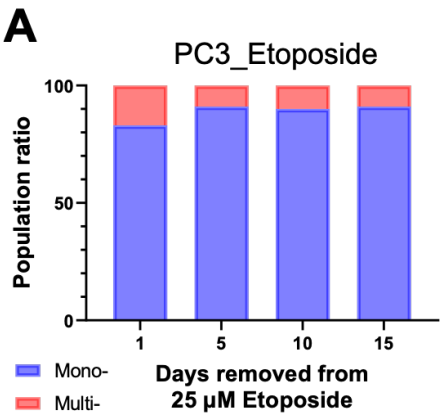

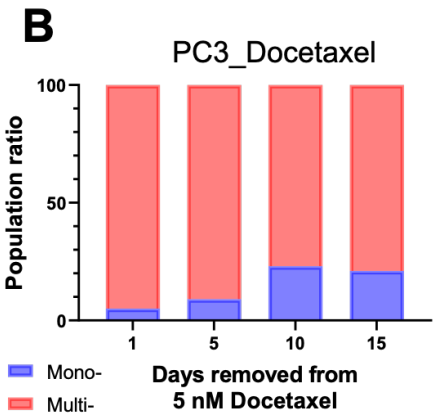

Figure S11. Nuclear morphology of treated PC3s generated with etoposide or docetaxel treatment. Population distribution of mononucleated and multinucleated treated PC3 cells generated with 72h **(A)** [LD50] etoposide treatment or **(B)** [LD50] docetaxel treatment, derived from immunofluorescent images of cells stained for lamin A/C and mounted with DAPI. Nuclear morphology (mononucleated vs. multinucleated) was discriminated and counted in Fiji software.

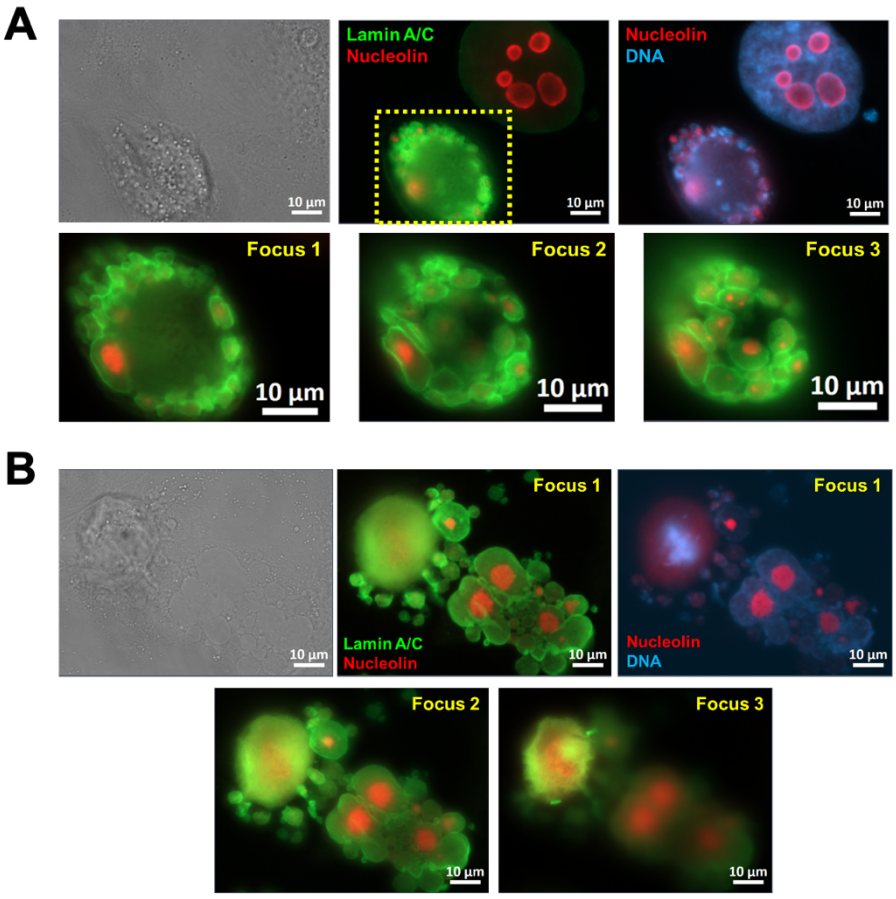

Figure S12. Effects of focal plane on morphologic discrimination of multinucleated cells. Treated PC3s induced with 72h [LD50] cisplatin treatment were stained for lamin A/C, nucleolin, and mounted with DAPI. **(A)** and **(B)** show two different examples of cells where the number of micronuclei/extent of multinucleation might be missed in 2D immunofluorescent microscopy due the effect of different focal planes and cell height.